



Combining radiative transfer and diffuse interstellar medium physics to model star formation

Matthew R. Bate^{1★} and Eric R. Keto^{2,3}

¹*School of Physics and Astronomy, University of Exeter, Stocker Road, Exeter EX4 4QL, UK*

²*Harvard–Smithsonian Center for Astrophysics, 160 Garden St, Cambridge, MA 02420, USA*

³*Max-Planck-Institut für Astronomie, Königstuhl 17, D-69117 Heidelberg, Germany*

Accepted 2015 February 26. Received 2015 February 26; in original form 2014 November 24

ABSTRACT

We present a method for modelling star-forming clouds that combines two different models of the thermal evolution of the interstellar medium (ISM). In the combined model, where the densities are low enough that at least some part of the spectrum is optically thin, a model of the thermodynamics of the diffuse ISM is more significant in setting the temperatures. Where the densities are high enough to be optically thick across the spectrum, a model of flux-limited diffusion is more appropriate. Previous methods either model the low-density ISM and ignore the thermal behaviour at high densities (e.g. inside collapsing molecular cloud cores), or model the thermal behaviour near protostars but assume a fixed background temperature (e.g. ≈ 10 K) on large scales. Our new method treats both regimes. It also captures the different thermal evolution of the gas, dust, and radiation separately. We compare our results with those from the literature, and investigate the dependence of the thermal behaviour of the gas on the various model parameters. This new method should allow us to model the ISM across a wide range of densities and, thus, develop a more complete and consistent understanding of the role of thermodynamics in the star formation process.

Key words: astrochemistry – hydrodynamics – radiative transfer – methods: numerical – stars: formation – ISM: general.

1 INTRODUCTION

The thermal behaviour of interstellar gas is of fundamental importance for star formation. To initiate star formation, the thermal pressure must be insufficient to support the gas against gravitational collapse (Jeans 1929). Further evolution also depends on the thermodynamics and density structure, with a variety of different outcomes being possible such as the formation of a single polytrope or fragmentation into many clouds (Hoyle 1953; Hunter 1962; Layzer 1963; Tohline 1980; Rozyczka 1983). Larson (1985, 2005) emphasized the importance of the relationship between temperature and density in the interstellar medium (ISM), and Whitworth, Boffin & Francis (1998) emphasized the importance of the transition from molecular cooling to dust cooling. The typical decrease in gas temperature from $T_g \sim 1000$ K at number densities of hydrogen nuclei of $n_H \sim 1 \text{ cm}^{-3}$ to $T_g \sim 10$ K at densities of $n_H \sim 10^4 \text{ cm}^{-3}$ promotes fragmentation, while the transition to an isothermal regime or temperature that increases with density above $n_H \sim 10^4 \text{ cm}^{-3}$ may help to produce a characteristic stellar mass (Larson 1985, 2005; Jappsen et al. 2005; Bonnell, Clarke & Bate 2006; Elmegreen, Klessen &

Wilson 2008). Chemical reactions that control the abundances of gas phase coolants, and therefore radiative equilibrium, may affect this transition and the formation of molecular cloud cores. At even higher densities, deep within collapsing molecular cloud cores, different phases of collapse are believed to occur as the gas becomes optically thick and later as molecular hydrogen dissociates (Larson 1969). The treatment of radiative transfer can be crucial for determining whether the core fragments into multiple protostars or not (Boss et al. 2000; Krumholz 2006; Whitehouse & Bate 2006).

Previous radiation hydrodynamical simulations of star cluster formation demonstrate the importance of radiative feedback from protostars to correctly capture fragmentation and produce realistic numbers of brown dwarfs (Bate 2009; Offner et al. 2009). Whereas barotropic calculations of star cluster formation produce characteristic stellar masses that depend on the initial Jeans mass in the cloud (Bate & Bonnell 2005), Bate (2009) showed that radiative feedback reduces this dependence on the initial conditions. This may help to explain the apparent universality of the stellar initial mass function (IMF), at least in recent epochs (see also Krumholz 2011). Indeed, some recent radiation hydrodynamical simulations of star cluster formation have been quite successful in reproducing the observed IMF and other properties of stellar systems (Bate 2012, 2014; Krumholz, Klein & McKee 2012).

* E-mail: mbate@astro.ex.ac.uk

However, to date, radiation hydrodynamical simulations of star formation have been restricted to modelling dense molecular clouds and assuming that the only significant sources of radiation are the protostars themselves. In this case, the gas temperature at large distances from the protostars is assumed to be ≈ 10 K. However, this approximation is generally invalid at densities $n_{\text{H}} \lesssim 10^4 \text{ cm}^{-3}$ with solar metallicities, and is invalid at even higher densities at lower metallicities, if at all.

Informed by the vast literature on the physics, thermodynamics, and chemistry of the diffuse ISM (see the thorough review provided by Tielens 2005) and collapsing clouds with different metallicities (e.g. Omukai 2000; Omukai et al. 2005), interest has grown in studying the formation and evolution of molecular clouds using three-dimensional hydrodynamical calculations coupled with chemistry. Initial calculations treated only the formation of molecular hydrogen (Dobbs, Bonnell & Pringle 2006; Dobbs & Bonnell 2007; Glover & Mac Low 2007a,b; Micic et al. 2012). More recent work has included more complex chemistry, in particular that involving carbon and oxygen (Glover et al. 2010; Glover & Mac Low 2011; Clark et al. 2012b; Glover & Clark 2012a,b,c). Along with the formation mechanisms of molecular clouds and their chemical and temperature distributions, some of these calculations have begun to investigate star formation, using sink particles to replace collapsing regions of gas (in particular, the models of Glover & Clark). At the same time, there have been several studies of the chemical and thermal evolution of low-metallicity clouds and their star formation (e.g. Dopcke et al. 2011, 2013; Glover & Clark 2012c).

Therefore, at the present time, the star formation community has two different classes of hydrodynamical models for star formation. One class treats the low-density thermochemical evolution in some detail, but does not treat radiative feedback from protostars. The other ignores the complicated physics of the diffuse ISM, which is particularly important at low densities and low metallicities, but includes the radiative effects of protostars. The goal of this paper is to make an attempt to bridge this gap, by combining a model for the physics of the low-density ISM with a method for modelling radiative transfer. Our main purpose is to develop a model that does a reasonable job of modelling the thermodynamics at both low and high densities in star-forming clouds, with metallicities as low as 1/100 solar. The aim is not to produce a detailed chemical model. Rather, we wish to implement the simplest possible chemical model that will provide the abundances of the major coolants of the gas that are necessary to calculate realistic temperatures.

It turns out that a method very similar to that which we present here has recently been developed by Pavlyuchenkov & Zhilkin (2013) and Pavlyuchenkov et al. (2015). Although we developed our method independently, each of the methods is based on extending a method of radiative transfer that is valid at high densities to include effects that are important at low densities. Each of the methods treats gas and dust temperatures separately. Pavlyuchenkov & Zhilkin (2013) base their method on the diffusion approximation for radiative transfer and add heating and cooling terms relevant at lower densities to model the collapse of dense molecular cloud cores. Pavlyuchenkov et al. (2015) replace the diffusion approximation with flux-limited diffusion like we use in this paper. They do not include cooling processes relevant at very low densities that we include (e.g. electron recombination and fine-structure emission from atomic oxygen), and they only perform one-dimensional calculations, but the underlying methods are very similar.

This paper is primarily a method paper where we describe our implementation and demonstrate its performance in a wide variety of tests, comparing our results to those of others who have performed

similar calculations (sometimes using much more complete and/or complex models). However, we also explore the effects of varying many of the parameters that go into the model in order to better understand which physical processes may be most important for affecting star formation. Large-scale star formation calculations are beyond the scope of this paper, but we hope to use this new method to perform such calculations in the future.

In Section 2, we provide the fundamental equations and assumptions that go into our model. The implementation of these equations into a smoothed particle hydrodynamics (SPH) code is described in Section 3. We present the results from our test calculations, and compare our results with those in the literature in Section 4. Finally, we draw our conclusions in Section 5.

2 METHOD

2.1 The flux-limited diffusion approximation

In a frame comoving with the fluid, and assuming local thermal equilibrium (LTE), the equations governing the time-evolution of radiation hydrodynamics (RHD) can be written as

$$\frac{D\rho}{Dt} + \rho \nabla \cdot \mathbf{v} = 0, \quad (1)$$

$$\rho \frac{D\mathbf{v}}{Dt} = -\nabla p + \frac{\chi_{\text{F}} \rho}{c} \mathbf{F}, \quad (2)$$

$$\rho \frac{D}{Dt} \left(\frac{E}{\rho} \right) = -\nabla \cdot \mathbf{F} - \nabla \mathbf{v} : \mathbf{P} + 4\pi \kappa_{\text{P}} \rho B - c \kappa_{\text{E}} \rho E, \quad (3)$$

$$\rho \frac{D}{Dt} \left(\frac{e}{\rho} \right) = -p \nabla \cdot \mathbf{v} - 4\pi \kappa_{\text{P}} \rho B + c \kappa_{\text{E}} \rho E \quad (4)$$

(Mihalas & Mihalas 1984; Turner & Stone 2001; Whitehouse, Bate & Monaghan 2005). In these equations, $D/Dt \equiv \partial/\partial t + \mathbf{v} \cdot \nabla$ is the convective derivative. The symbols ρ , e , \mathbf{v} , and p represent the material mass density, energy density, velocity, and scalar isotropic pressure, respectively, and c is the speed of light. The total frequency-integrated radiation density, momentum density (flux) and pressure tensor are represented by E , \mathbf{F} , and \mathbf{P} , respectively. The assumption of LTE allows the rate of emission of radiation from the matter in equations (3) and (4) to be written as the frequency-integrated Planck function, B . Equations (2)–(4) have been integrated over frequency, leading to the flux mean total opacity χ_{F} , and the Planck mean and energy mean absorption opacities, κ_{P} and κ_{E} . The total opacity, χ , is the sum of components due to absorption κ and scattering σ .

Taking an ideal equation of state for the gas pressure $p = (\gamma - 1)u\rho$, where $u = e/\rho$ is the specific energy of the gas, the temperature of the gas is $T_{\text{g}} = (\gamma - 1)\mu u/\mathcal{R}$, where μ is the mean molecular weight of the gas and \mathcal{R} is the gas constant. The frequency-integrated Planck function is given by $B = (\sigma_{\text{B}}/\pi)T_{\text{g}}^4$, where σ_{B} is the Stefan–Boltzmann constant. The radiation energy density also has an associated temperature T_{r} from the equation $E = 4\sigma_{\text{B}}T_{\text{r}}^4/c$.

A common approximation to make in RHD is the so-called flux-limited diffusion approximation. For an isotropic radiation field $\mathbf{P} = E\mathbf{I}/3$. The Eddington approximation assumes this relation holds everywhere and implies that, in a steady state,

$$\mathbf{F} = -\frac{c}{3\chi\rho} \nabla E. \quad (5)$$

This expression gives the correct flux in optically thick regions, where $\chi\rho$ is large. However, in optically thin regions where $\chi\rho \rightarrow 0$, the flux tends to infinity whereas in reality $|\mathbf{F}| \leq cE$. Flux-limited diffusion solves this problem by limiting the flux in optically thin environments to always obey this inequality. Levermore & Pomraning (1981) wrote the radiation flux in the form of Fick's law of diffusion as

$$\mathbf{F} = -D\nabla E, \quad (6)$$

with a diffusion constant given by

$$D = \frac{c\lambda}{\chi\rho}. \quad (7)$$

The dimensionless function $\lambda(E)$ is called the flux limiter. The radiation pressure tensor may then be written in terms of the radiation energy density as

$$\mathbf{P} = fE, \quad (8)$$

where the components of the Eddington tensor, f , are given by

$$f = \frac{1}{2}(1-f)\mathbf{I} + \frac{1}{2}(3f-1)\hat{n}\hat{n}, \quad (9)$$

where $\hat{n} = \nabla E/|\nabla E|$ is the unit vector in the direction of the radiation energy density gradient and the dimensionless scalar function $f(E)$ is called the Eddington factor. The flux limiter and the Eddington factor are related by

$$f = \lambda + \lambda^2 R^2, \quad (10)$$

where R is the dimensionless quantity $R = |\nabla E|/(\chi\rho E)$.

Equations (6)–(10) close the equations of RHD. However, we must still choose an expression for the flux limiter, λ . In this paper, we choose the flux limiter of Levermore & Pomraning (1981):

$$\lambda(R) = \frac{2+R}{6+3R+R^2}. \quad (11)$$

There are a number of problems with using the flux-limited diffusion approximation to model radiative processes in star formation. Many of these are a direct result of the approximations made in deriving the method. The diffusion approximation is good at high optical depths, but the directional behaviour of anisotropic radiation at low optical depths is modelled poorly. This means, for example, that shadowing is not reproduced. The flux limiter gives the correct limiting behaviour for the propagation rate in the optically thin and thick regimes, but at intermediate optical depths is dependent on the arbitrary choice of the flux limiter. Finally, most implementations take the grey approach, ignoring the frequency dependence of the radiative transfer in favour of mean opacities (as discussed above). This is likely to be a good approximation when most of the energy is in long-wavelength radiation, but is a poor approximation near hot massive stars (Wolfire & Cassinelli 1987; Preibisch, Sonnhalter & Yorke 1995; Yorke & Sonnhalter 2002; Edgar & Clarke 2003).

Despite these drawbacks, flux-limited diffusion is expected to do a reasonable job of modelling radiative transfer in dense star-forming regions that produce low-mass stars (e.g. Bate 2009, 2012; Offner et al. 2009), and it is computationally efficient.

2.2 The diffuse ISM

However, other problems arise when modelling low-density environments. For a start, the above-mentioned equations treat radiation and matter, but do not distinguish between different types of matter which may have different temperatures. In particular, at solar

metallicities, dust and gas temperatures are only well coupled (by collisions) at gas densities above 10^5 cm^{-3} (Burke & Hollenbach 1983; Goldsmith 2001; Glover & Clark 2012a). At lower densities, the gas and dust temperatures can be very different from one another with the gas temperature typically exceeding that of the dust. There are also sources of heating that affect the matter other than work done on the gas and the radiative interaction between the matter and the radiation field that are included in equation (4). Cosmic rays heat the gas by direct collision (Goldsmith, Habing & Field 1969; O'Donnell & Watson 1974; Black & Dalgarno 1977; Goldsmith & Langer 1978). Ultraviolet (UV) photons heat the gas indirectly through the photoelectric release of hot electrons from dust grains (Draine 1978; Bakes & Tielens 1994). Absorption and emission of radiation that is highly frequency dependent is also problematic in a grey treatment. In particular, gas cooling occurs by atomic and molecular line cooling which may be optically thin due to Doppler shifts even when static clouds would be optically thick. The external interstellar radiation (ISR) field (Habing 1968; Witt & Johnson 1973; Draine 1978; Black 1994), attenuated by dust extinction, also heats the dust.

2.3 Combining a diffuse ISM model with flux-limited diffusion

In this section, we present a method to combine a model of the radiative equilibrium of the diffuse ISM with flux-limited diffusion to determine the gas, dust, and radiation temperatures in both low-density and high-density regions of molecular clouds. We include treatments for all of the effects mentioned in the previous section. We also allow for heating due to H_2 formation. We do not treat photoionization or heating from X-rays.

We use equations (2)–(4) to model the continuum radiation field and the gas, and add extra terms to handle cosmic ray heating, the photoelectric effect, and radiation that is strongly frequency dependent. We replace equations (3) and (4) with

$$\rho \frac{D}{Dt} \left(\frac{E}{\rho} \right) = -\nabla \cdot \mathbf{F} - \nabla \mathbf{v} : \mathbf{P} - ac\kappa_g \rho (T_r^4 - T_g^4) - ac\kappa_d \rho (T_r^4 - T_d^4), \quad (12)$$

$$\rho \frac{Du}{Dt} = -p\nabla \cdot \mathbf{v} + ac\kappa_g \rho (T_r^4 - T_g^4) - \Lambda_{\text{gd}} - \Lambda_{\text{line}} + \Gamma_{\text{cr}} + \Gamma_{\text{pe}} + \Gamma_{\text{H}_2, \text{g}}, \quad (13)$$

where equation (13) now describes the evolution of the specific internal energy of the gas, u , separately from the dust. The extra terms at the end of equation (13) are Λ_{gd} which takes account of the thermal interaction due to collisions between the gas and the dust, Λ_{line} is the cooling rate per unit volume due to atomic and molecular line emission, Γ_{cr} is the heating rate per unit volume due to cosmic rays, Γ_{pe} is the heating rate per unit volume due to the photoelectric effect, and $\Gamma_{\text{H}_2, \text{g}}$ is the heating rate per unit volume due to the formation of molecular hydrogen on dust grains. We also define the radiation constant $a = 4\sigma_{\text{B}}/c$ and the dust temperature T_d . We define the Rosseland mean gas opacity κ_g (which is only important above the dust sublimation temperature) and the mean dust opacity κ_d , which may be a Planck mean or Rosseland mean (see Section 3.3).

We still need to determine the dust temperature. As done in most studies of the thermal structure of molecular clouds (e.g. Goldsmith 2001), we assume that the dust is in LTE with the total radiation field (i.e. that its temperature responds quickly to any change). This

replaces a dust thermal energy equation (which would also require the thermodynamic properties of the dust). Thus, we take

$$\rho \Lambda_{\text{ISR}} + ac\kappa_d \rho (T_r^4 - T_d^4) + \Lambda_{\text{gd}} = 0, \quad (14)$$

where Λ_{ISR} is the heating of the dust due to the ISR field (which is taken to be separate from the grey radiation field with temperature T_r). By rearranging equation (14) for Λ_{gd} and eliminating this term from equation (13), it is easy to show that equations (12) and (13) reduce to equations (3) and (4) when $T_d = T_g$ and $\Lambda_{\text{line}} = \Lambda_{\text{gd}} = \Gamma_{\text{cr}} = \Gamma_{\text{pe}} = \Gamma_{\text{H}_2, \text{g}} = 0$, and where $\kappa_P \rho = (\kappa_d + \kappa_g) \rho$ and $\kappa_P = \kappa_E$.

We note that the dust cooling rate

$$\begin{aligned} \Lambda_{\text{dust}} &= ac\kappa_d T_d^4 = 4\sigma_B \left(\int Q_\nu B_\nu d\nu \right) \frac{\pi}{\sigma_B T_d^4} T_d^4, \\ &= 4\pi \int Q_\nu B_\nu d\nu, \end{aligned} \quad (15)$$

where ν is the frequency of the radiation, and Q_ν is the frequency-dependent dust absorption efficiency. Therefore, when $\Lambda_{\text{gd}} = 0$, and $T_r = 0$, and in the absence of extinction, the thermal balance with the ISR is obtained when

$$\Lambda_{\text{dust}} = \Lambda_{\text{ISR}} = 4\pi \int Q_\nu J_\nu^{\text{ISR}} d\nu, \quad (16)$$

where J_ν^{ISR} is the frequency-dependent ISR field.

We note that equations 12 and 13 in Goldsmith (2001) appear to be incorrect. It is stated that the dust cooling rate is given by

$$\Lambda_{\text{dust}} = c \int U_\nu(T_d) \kappa(\nu) d\nu, \quad (17)$$

where $U_\nu(T)$ is the Planck energy density and where they took

$$\kappa(\nu) = 3.3 \times 10^{-26} n_{\text{H}_2} (\nu/\nu_0)^2 \text{ cm}^{-1}, \quad (18)$$

with $\nu_0 = 3.8 \times 10^{11}$ Hz, and n_{H_2} is the number density of molecular hydrogen. However, we can write

$$\begin{aligned} \Lambda_{\text{dust}} &= c \int U_\nu(T_d) \kappa(\nu) d\nu = 4\pi \int B_\nu(T_d) \kappa(\nu) d\nu, \\ &= \frac{3.3 \times 10^{-26} n_{\text{H}_2} 4\pi}{\nu_0^2} \int \frac{2h\nu^5}{c^2} \frac{1}{e^{h\nu/(kT_d)} - 1} d\nu, \\ &= \frac{3.3 \times 10^{-26} n_{\text{H}_2} 8\pi h}{\nu_0^2 c^2} \int \nu^5 \frac{1}{e^{h\nu/(kT_d)} - 1} d\nu, \\ &= \frac{3.3 \times 10^{-26} n_{\text{H}_2} 8\pi}{\nu_0^2 c^2} \frac{k^6 T_d^6}{h^5} \int s^5 \frac{1}{e^s - 1} ds, \end{aligned} \quad (19)$$

where h is the Planck constant, k is Boltzmann's constant, and we have written $s = h\nu/(kT_d)$. The integral can be performed over all frequencies, and can be evaluated as

$$\int_0^\infty \frac{s^5}{e^s - 1} ds = \Gamma(6)\zeta(6) = 5!\zeta(6) = \frac{8\pi^6}{63} \approx 122.08, \quad (20)$$

where $\Gamma(n) = (n-1)!$ is the Gamma function and the Riemann zeta function, $\zeta(2n)$, can be evaluated as

$$\zeta(2n) = \frac{(-1)^{n+1} B_{2n} (2\pi)^{2n}}{2(2n)!} \quad (21)$$

so that

$$\zeta(6) = \frac{(-1)^4 B_6 (2\pi)^6}{2(6)!} = \frac{\pi^6}{945}, \quad (22)$$

where B_{2n} is a Bernoulli number and $B_6 = 1/42$. Thus,

$$\begin{aligned} \Lambda_{\text{dust}} &= \frac{3.3 \times 10^{-26} n_{\text{H}_2} 8\pi}{\nu_0^2 c^2} \frac{k^6 T_d^6}{h^5} 122.08, \\ &= 4.22 \times 10^{-31} n_{\text{H}_2} T_d^6 \text{ erg cm}^{-3} \text{ s}^{-1}. \end{aligned} \quad (23)$$

This is a factor of ≈ 62 times larger (probably $2^6 = 64$) than equation 13 in Goldsmith (2001) which states $\Lambda_{\text{dust}} = 6.8 \times 10^{-33} n_{\text{H}_2} T_d^6$. The effect of the greater dust cooling rate is to lower the dust temperatures by a factor of 2 for a given ISR field. We note that Glover & Clark (2012b) use $\Lambda_{\text{dust}} = 4.68 \times 10^{-31} n_{\text{H}_2} T_d^6$, which only differs from equation (23) by 10 per cent (presumably due to the choice of different dust opacities).

2.4 Equations for heating and cooling terms in the ISM

To calculate the extra heating and cooling terms appearing in equations (12)–(14), we make the same approximations as those made in the past by many others who have studied the thermal structure of molecular clouds.

2.4.1 Gas heating equations

Following Goldsmith (2001) and Keto & Field (2005), we set the rate of energy transfer from cosmic rays into the gas as

$$\Gamma_{\text{cr}} = 5 \times 10^{-28} n_{\text{H}} \text{ erg cm}^{-3} \text{ s}^{-1}. \quad (24)$$

Note that Goldsmith (2001) and Keto & Field (2005) express their rates as functions of $n_{\text{H}_2} = n_{\text{H}}/2$ for molecular gas. We will usually refer to n_{H} throughout this paper, since when we allow for both atomic and molecular hydrogen the meaning of n_{H_2} may not be clear.

The ISR is used to determine both the heating rate of the dust grains, and the photoelectric heating rate of the gas. In both cases, the ISR is attenuated due to dust extinction inside a molecular cloud. To describe the ISR, we use a slight modification to that described in detail by Zucconi, Walmsley & Galli (2001). They made approximate fits to the ISR given by Black (1994) using the sum of a power-law distribution and five modified blackbody distributions of the form

$$J_\nu^{\text{ISR}} = \frac{2h\nu^3}{c^2} \left(\frac{\lambda_p}{\lambda} \right)^p \sum_i \frac{W_i}{e^{h\nu/kT_i} - 1}, \quad (25)$$

where λ is the wavelength of the radiation, and the parameters λ_p , W_i , and T_i are given in their table B.1. Note that the mid-infrared term in their ISR is a power law with a cut-off longwards of 100 μm (which is mentioned in the main text of the paper, but not in their appendix). Although the Zucconi et al. (2001) parametrization does a good job of fitting Black's ISR at most wavelengths, it does not provide a significant UV flux which is necessary for photoelectric heating. To allow us to use one ISR parametrization for both dust heating and the photoelectric effect, we add the 'standard' UV background from equation 11 of Draine (1978) but only in the range $h\nu = 5\text{--}13.6$ eV. Note that to transform Draine's parametrization into the same units as equation (25), it must be multiplied by $h^2\nu/\text{eV}$.

For the photoelectric heating, we follow the prescription of Bakes & Tielens (1994), which has also been used by Young et al. (2004) and Keto & Caselli (2008), that

$$\Gamma_{\text{pe}} = 1.33 \times 10^{-24} \epsilon G(\mathbf{r}) n_{\text{H}} \text{ erg cm}^{-3} \text{ s}^{-1}, \quad (26)$$

where, as described by Young et al. (2004), we have assumed that the number density of nucleons $n_n \approx n_H + 4n(\text{He})$ and that the gas is 25 per cent helium by mass so that $n_n = 1.33n_H$. The quantity $G(\mathbf{r})$ is the ratio of the attenuated intensity of high-energy ($h\nu > 6 \text{ eV}$) photons to their unattenuated intensity

$$G(\mathbf{r}) = \frac{\int_0^{4\pi} \int_{6 \text{ eV}}^{\infty} J_v^{\text{ISR}} \exp[-\tau_v(\mathbf{r}, \omega)] \text{d}\nu \text{d}\Omega}{\int_0^{4\pi} \int_{6 \text{ eV}}^{\infty} J_v^{\text{ISR}} \text{d}\nu \text{d}\Omega}, \quad (27)$$

where $\tau_v(\mathbf{r}, \omega)$ is the frequency-dependent optical depth from \mathbf{r} to the cloud surface along direction, ω , and Ω is solid angle. The efficiency factor ϵ is a complicated function of the type of dust grains, radiation intensity, $G(\mathbf{r})$, the temperature, and the electron number density. We use equation 43 of Bakes & Tielens (1994)

$$\epsilon = \frac{0.049}{1 + 4 \times 10^{-3} [G(\mathbf{r}) T_g^{1/2} / (n_e \phi_{\text{PAH}})]^{0.73}} + \frac{0.037 (T_g / 10^4)^{0.7}}{1 + 2 \times 10^{-4} [G(\mathbf{r}) T_g^{1/2} / (n_e \phi_{\text{PAH}})]}, \quad (28)$$

but with the adjustable parameter ϕ_{PAH} that was introduced by Wolfire et al. (2003). We follow Wolfire et al. (2003) and use $\phi_{\text{PAH}} = 0.55$ whereas the original equation of Bakes & Tielens (1994) had $\phi_{\text{PAH}} = 1$. For the conditions in cold molecular clouds, the efficiency factor is nearly constant and can be approximated as $\epsilon = 0.05$ (note that in Keto & Caselli 2008, there is a typographical error giving $\epsilon = 0.5$, and they also neglect the factor of 1.33 in Γ_{pe}). However, it is important to use the more complicated form at the lower densities of the warm and cold neutral mediums. Ordinarily, the electron number density, n_e , would come from a chemical model, but because we do not have such a model we need to parametrize it. Using the results of Wolfire et al. (2003), in particular those displayed in their fig. 10, we use the simple parametrization

$$n_e = n_H \max(1 \times 10^{-4}, \min(1, 0.008/n_H)). \quad (29)$$

2.4.2 Gas cooling equations

We develop a model for cooling in the diffuse ISM based on the results of the detailed model developed by Wolfire et al. (2003, see also Glover & Mac Low 2007a). In the warm neutral medium (WNM), with a characteristic temperature of $T \sim 8000 \text{ K}$, cooling is dominated by Ly α emission from atomic hydrogen, electron recombination with small grains and polycyclic aromatic hydrocarbons (PAHs), and fine-structure emission from atomic oxygen. At temperatures between those of the WNM and the cold neutral medium (CNM; $T \lesssim 300 \text{ K}$), oxygen emission continues to contribute significant cooling but fine-structure emission from ionized carbon also becomes important and dominates in the colder parts of the CNM. Unlike Wolfire et al. (2003) and Glover & Mac Low (2007a), our aim is to achieve realistic temperatures without having to develop a detailed chemical model. Since we are not interested in regions of the ISM with temperatures greater than those of the WNM, we can produce a reasonable fit to the thermal behaviour by treating only the electron recombination, oxygen, and carbon emission. Following Wolfire et al. (2003) and Glover & Mac Low (2007a), we use the modified formula of Bakes & Tielens (1994)

$$\Lambda_{\text{rec}} = 4.65 \times 10^{-30} \phi_{\text{PAH}} T_g^{0.94} \varphi^\beta n_e n_H \text{ erg cm}^{-3} \text{ s}^{-1}, \quad (30)$$

where $\beta = 0.74/T_g^{0.068}$, and

$$\varphi = \frac{G(\mathbf{r}) T_g^{1/2}}{n_e \phi_{\text{PAH}}}. \quad (31)$$

For the atomic oxygen fine-structure cooling, we use equation C3 of Wolfire et al. (2003)

$$\Lambda_{\text{OI}} = 2.5 \times 10^{-27} n_H^2 \left(\frac{T_g}{100 \text{ K}} \right)^{0.4} \exp\left(\frac{-228}{T_g} \right) \text{ erg cm}^{-3} \text{ s}^{-1}. \quad (32)$$

Keto, Rawlings & Caselli (2014) calculate the cooling taking into account the abundance of atomic oxygen.

For the atomic carbon fine-structure cooling, we use equation C1 of Wolfire et al. (2003)

$$\Lambda_{\text{C}^+} = 3.15 \times 10^{-27} n_H^2 \exp\left(\frac{-92}{T_g} \right) \text{ erg cm}^{-3} \text{ s}^{-1}, \quad (33)$$

which assumes a carbon abundance relative to hydrogen of $\mathcal{A}_C = 1.4 \times 10^{-4}$. This is almost identical to equation of 2.67 of Tielens (2005), which was also used by Keto & Caselli (2008), except that in equation (33) the dependence on the degree of ionization, X_i , has been neglected. Keto & Caselli (2008) assume that the degree of ionization is equal to the abundance of C^+ with respect to H_2 .

At the low densities of the WNM and CNM, the equations for cosmic ray and photoelectric heating and cooling due to electron recombination and oxygen and carbon cooling can be used to calculate the equilibrium temperature as a function of density. This equilibrium curve resulting from our chosen parametrizations is shown in Fig. 1 as the solid line and compared to the results obtained by Wolfire et al. (2003) for solar metallicities at a Galactic radius of 8.5 kpc using a dashed line. Given that our model is much simpler than that of Wolfire et al. (2003) and that our main interest is in the star formation occurring in higher density ($n_H \gtrsim 100 \text{ cm}^{-3}$)

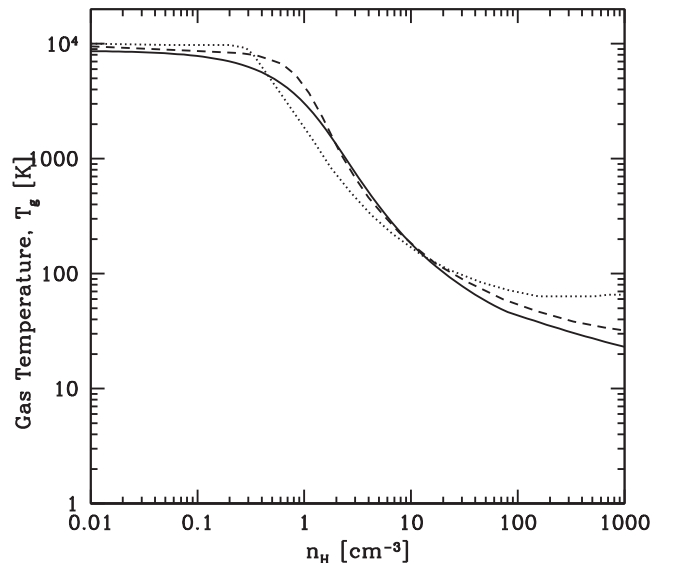


Figure 1. The equilibrium temperature as a function of the number density of hydrogen nuclei, n_H , in the warm and cold neutral mediums achieved by considering cosmic ray and photoelectric heating (without extinction) balanced by cooling due to electron recombination, and fine-structure emission from carbon and oxygen (solid line; equations 24, 26, 30, 32, and 33). The dashed line gives the result obtained by Wolfire et al. (2003) for solar metallicity gas at a Galactic radius of 8.5 kpc. The dotted line gives the result from the model of Glover & Mac Low (2007a).

molecular gas where other processes dominate, the level of agreement is satisfactory. Also plotted in the figure with a dotted line is the result obtained by Glover & Mac Low (2007a). We note that our model gives slightly lower temperatures than Wolfire et al. (2003) at densities $n_{\text{H}} \gtrsim 20 \text{ cm}^{-3}$, while the model of Glover & Mac Low (2007a) gives somewhat higher temperatures.

For the molecular line cooling, we follow Keto & Field (2005) by using the parametrized cooling functions provided by Goldsmith (2001) for standard abundances given by

$$\Lambda_{\text{line}} = \alpha(T_{\text{g}}/10\text{K})^{\beta} \text{ erg cm}^{-3} \text{ s}^{-1}, \quad (34)$$

where the parameters α and β are given in tables in Goldsmith (2001) as functions of n_{H_2} (we take $n_{\text{H}_2} = n_{\text{H}}/2$). We allow the possibility of performing calculations both with standard abundances and with depleted abundances. In the former case, table 2 of Goldsmith (2001) gives cooling rates without allowing for depletion on to grains and covers the range $n_{\text{H}_2} = 10^2\text{--}10^7 \text{ cm}^{-3}$. We tried using linear interpolation of the logarithm of the cooling rates at the given points to compute the cooling rate at a particular value of n_{H_2} , but found that this tended to give discontinuities in the temperature gradients in molecular cloud cores. Instead, we use three-point polynomial interpolation of the logarithm of the cooling rate (taking one point at the nearest tabulated value of n_{H_2} below the required density and two points above the required density, except for the highest densities where the reverse is done). This works well over the entire range of n_{H_2} except that it gives a ‘bulge’ in the cooling rate in the range $n_{\text{H}_2} = 10^3\text{--}10^4 \text{ cm}^{-3}$. To fix this, in this range, we calculate two three-point polynomial interpolations (one that has one point below the required value of n_{H_2} and two points above, and the other that has two tabulated values below and one above) and then use linear interpolation of the logarithm of these two values to obtain the cooling rate. At densities $n_{\text{H}_2} < 10^2 \text{ cm}^{-3}$, we extrapolate the line cooling rate using the three-point polynomial derived from the first three points in the table. At densities $n_{\text{H}_2} > 10^8 \text{ cm}^{-3}$, we set the line cooling to zero (since it will be negligible compared to the other heating and cooling terms anyway).

To allow for depletion, we use table 4 of Goldsmith (2001) which gives cooling rates as functions of density over the range $n_{\text{H}_2} = 10^3\text{--}10^6 \text{ cm}^{-3}$ and as functions of a depletion factor ranging from 1 to 100. When depletion is allowed, for $n_{\text{H}_2} < 10^2 \text{ cm}^{-3}$ we use the standard cooling rates divided by the depletion factor, and for $n_{\text{H}_2} > 10^7 \text{ cm}^{-3}$ we use the standard cooling rates (since the cooling rates become less dependent on the depletion factor at high densities, according to Goldsmith 2001). In the intermediate density range, we use bilinear interpolation in log-space of the values in table 4 that are given as functions of density and depletion. In the ranges $n_{\text{H}_2} = 10^2\text{--}10^3 \text{ cm}^{-3}$ and $n_{\text{H}_2} = 10^6\text{--}10^7 \text{ cm}^{-3}$, we further use linear interpolation in log-space to achieve smooth transitions between using the depleted cooling rates (from table 4) and the depleted standard cooling rates ($n_{\text{H}_2} = 10^2\text{--}10^3 \text{ cm}^{-3}$) or the standard cooling rates ($n_{\text{H}_2} = 10^6\text{--}10^7 \text{ cm}^{-3}$).

2.4.3 Dust heating and cooling equations

For the heating rate of dust grains, we follow Zucconi et al. (2001) and Keto & Field (2005) and calculate the grain heating due to an incident radiation field whose intensity is attenuated by the optical depth averaged over 4π steradians upon grains of the absorption efficiency, Q_{v} . Thus,

$$\Lambda_{\text{ISR}} = \int_0^{4\pi} \int_0^{\infty} Q_{\text{v}} J_{\text{v}}^{\text{ISR}} \exp[-\tau_{\text{v}}(\mathbf{r}, \omega)] \text{d}\nu \text{d}\Omega, \quad (35)$$

where $\tau_{\text{v}}(\mathbf{r}, \omega)$ is the frequency-dependent optical depth from \mathbf{r} to the cloud surface along direction, ω , and we have deliberately omitted to normalize the integral over solid angle because of equation (16). Zucconi et al. (2001) defines Q_{v} in units of $\text{cm}^2 \text{ H}_2^{-1}$, but in the above-mentioned equation we redefine Q_{v} to be in units of $\text{cm}^2 \text{ g}^{-1}$ by dividing by μm_{p} , where m_{p} is the proton mass. For simplicity, we use the parametrization of Q_{v} given by Zucconi et al. (2001). See Section 3.3 for more information regarding the opacities we use.

The thermal interaction between the gas and the dust depends sensitively on the distribution of grain sizes (Burke & Hollenbach 1983). We use two different rates in Section 4, depending on which tests we are performing. For most of the calculations, we use the rate of Keto & Field (2005)

$$\Lambda_{\text{gd}} = 2.5 \times 10^{-34} n_{\text{H}}^2 T_{\text{g}}^{1/2} (T_{\text{g}} - T_{\text{d}}) \text{ erg cm}^{-3} \text{ s}^{-1}, \quad (36)$$

which is similar to that used by Goldsmith (2001) (our rate is a factor of $\sqrt{10}/2 \approx 1.6$ larger). However, this rate is more than an order of magnitude smaller than the rate given in equation 2.15 of Hollenbach & McKee (1989)

$$\Lambda_{\text{gd}} = 3.8 \times 10^{-33} n_{\text{H}}^2 T_{\text{g}}^{1/2} (T_{\text{g}} - T_{\text{d}}) \times \left[1 - 0.8 \exp\left(\frac{-75}{T_{\text{g}}}\right) \right] \text{ erg cm}^{-3} \text{ s}^{-1}, \quad (37)$$

assuming a minimum grain size of $0.01 \mu\text{m}$. The last term in this equation takes account of the effects of the contributions of gas species other than protons and the effects of particle and grain charges. This is the rate used by Glover & Clark (2012b), so we use this rate for the tests in Section 4.4.

2.4.4 Metallicity

In all of the above-mentioned equations, we have assumed standard abundances and gas-to-dust mass ratios. To allow the modelling of molecular gas with different metallicities, we assume that Q_{v} (and hence κ_{d}), Λ_{gd} , Λ_{line} , and Γ_{pe} all scale linearly with the metallicity. Thus, each of these quantities is multiplied by the factor Z/Z_{\odot} . In doing so, we are also assuming that the grain properties are independent of the metallicity. Note that Γ_{cr} does not depend on the metallicity. Also, the gas opacities, κ_{g} , already explicitly include the metallicity dependence (see Section 3.3).

2.5 Chemistry

As mentioned in the Introduction, our aim with this method is to develop a relatively simple model that captures the most important thermodynamic behaviour of the low-density ISM, not to develop a full chemical model of molecular clouds. The equations in the previous section almost enable us to do this without modelling any chemistry at all. However, as we will see in Section 4.4, we do need to have some model to treat the transformation of C^+ into CO. At low densities ($n_{\text{H}} \approx 10\text{--}10^3 \text{ cm}^{-3}$) C^+ is the major coolant, while at higher densities CO is the primary coolant until dust takes over (e.g. Glover & Clark 2012b). Furthermore, particularly at low metallicities, extra heating of the gas can be provided by the formation of molecular hydrogen so we need to treat the evolution of atomic and molecular hydrogen.

2.5.1 Carbon chemistry

Keto & Caselli (2008) provide a very simple model of the abundances of C^+ , neutral carbon, and CO, including the depletion of CO on to dust grains. Glover & Clark (2012b) show that the model significantly underestimates the abundance of neutral carbon, but this is only important in a narrow density range around $n_H \approx 10^3 \text{ cm}^{-3}$ and is unimportant for cooling (Glover & Clark 2012a). Therefore, we implement the model of Keto & Caselli as stated in their paper, except as noted by Glover & Clark (2012b) there is a typographical error in equation 5 of Keto & Caselli (2008) which should read

$$\frac{CO}{C^+} = \frac{6 \times 10^{-16} n_{H_2}}{1.4 \times 10^{-11} G_0 \exp(-3.2A_V)}, \quad (38)$$

where G_0 is the ISR field in units of the Habing flux (Habing 1968) and we take $G_0 = 1$.

The only significant extra quantity that we need to calculate in order to implement the chemical model of Keto & Caselli is the mean visual extinction

$$\langle \exp(-A_V) \rangle = \frac{1}{4\pi} \int \exp(-A_V) d\Omega, \quad (39)$$

where we take $A_V = \Sigma Q_V(V)$, where Σ is the column density in g cm^{-2} (so if the hydrogen is fully molecular the column density of H_2 is $N_{H_2} = \Sigma / [\mu m_H]$) and we take the frequency of visual light to be that of light with a wavelength of 550 nm. This is calculated at the same time as the integrals in equations (35) and (27) (see Section 3.1.2). We use the resulting C^+ abundance to scale the fine-structure carbon cooling in equation (33), and we use the CO depletion factor that the model provides as the depletion value to use for the line cooling of Goldsmith (2001).

2.5.2 Hydrogen chemistry

For the hydrogen chemistry, we only consider H_2 formation on grains and dissociation due to cosmic rays and photodissociation. Omukai (2000) finds that grain formation dominates over gas phase formation (i.e. via H^- or H_2^+ ions) for metallicities $Z/Z_\odot \gtrsim 10^{-4}$. Glover (2003) compares gas-phase and grain-catalysed formation in detail and draws similar conclusions – for temperatures less than a few hundred kelvin, H_2 formation on grains is expected to dominate for dust-to-gas ratios $\gtrsim 10^{-3}$ – 10^{-4} of that found in the local ISM, over wide ranges of densities and levels of ionization. We neglect collisional dissociation of H_2 as at the temperatures we are dealing with in the low-density ISM it is expected to be negligible compared to photodissociation and dissociation due to cosmic rays (cf. the rates in Lepp & Shull 1983).

In the previous sections, when we have used n_{H_2} , it has been in the context of fully molecular gas for which $n_{H_2} = n_H/2$. However, with the introduction of hydrogen chemistry, we need to distinguish between atomic and molecular hydrogen. We therefore introduce the fraction of molecular hydrogen, x_{H_2} , which is equal to $n_{H_2}/n_H = 1/2$ when the gas is fully molecular, and is equal to zero when the gas is fully atomic.

For the formation rates of H_2 on grains, and the dissociation due to cosmic rays and photodissociation, we use the same model as Glover et al. (2010). The formation rate is given by equation 165 in table B1 of Glover et al. (2010), which is

$$R_{H_2} = 3.0 \times 10^{-18} T_g^{0.5} f_A f_B (Z/Z_\odot) \text{ cm}^3 \text{ s}^{-1}, \quad (40)$$

where we have assumed that the rate scales linearly with the metallicity due to the variation in the grain abundance, and where

$$f_A = [1.0 + 10^4 \exp(-600/T_d)]^{-1}, \quad (41)$$

$$f_B = [1.0 + 0.04(T_g + T_d)^{0.5} + 0.002T_g + 8 \times 10^{-6} T_g^2]^{-1}. \quad (42)$$

The number density of H_2 then evolves as

$$\left. \frac{dn_{H_2}}{dt} \right|_{\text{form}} = R_{H_2} [n_H (1 - 2x_{H_2})]^2. \quad (43)$$

For the magnitude of the dissociation of molecular hydrogen due to cosmic rays, we use the rate given in table 2 of Bergin et al. (2004)

$$\left. \frac{dn_{H_2}}{dt} \right|_{\text{cr}} = 1.2 \times 10^{-17} x_{H_2} n_H \text{ cm}^{-3} \text{ s}^{-1}. \quad (44)$$

For photodissociation of molecular hydrogen, we use the same model as Glover & Mac Low (2007a) and Glover et al. (2010), which is based on the work of Draine & Bertoldi (1996). We take the photodissociation rate of H_2 in optically thin gas to be

$$R_{\text{pd},0} = 5.6 \times 10^{-11} \text{ s}^{-1}, \quad (45)$$

where we have assumed a Draine (1978) UV ISR field. We take into account attenuation of the radiation due to dust absorption, and also self-shielding of the H_2 by line absorption due to other H_2 molecules. For the former, we use

$$f_{\text{dust}} = \langle \exp(-A_V) \rangle^{3.74}, \quad (46)$$

which is simply a power of the mean visual extinction that is already required for the carbon chemistry (equation 39). For the self-shielding, we use

$$f_{\text{shield}} = \frac{0.965}{(1 + x/b_5)^2} + \frac{0.035}{(1 + x)^{1/2}} \exp[-8.5 \times 10^{-4} (1 + x)^{1/2}], \quad (47)$$

where $x = N_{H_2}/(5 \times 10^{14} \text{ cm}^{-2})$, and $b_5 = b/(10^5 \text{ cm s}^{-1})$ with b being the Doppler broadening parameter (which we take to be unity in the tests below). The magnitude of the fully shielded H_2 photodissociation rate is then

$$\left. \frac{dn_{H_2}}{dt} \right|_{\text{pd}} = R_{\text{pd},0} f_{\text{dust}} f_{\text{shield}} x_{H_2} n_H. \quad (48)$$

Once the total rate of change of molecular hydrogen has been obtained, the rate of change of the H_2 fraction is evolved as

$$\frac{dx_{H_2}}{dt} = \frac{1}{n_H} \frac{dn_{H_2}}{dt}. \quad (49)$$

The formation of molecular hydrogen on dust grains releases approximately 4.5 eV of energy per molecule. A fraction of this will be radiatively lost while the remainder will heat the gas, with the relative fractions depending on the collisional de-excitation rate which depends on density. Following Glover & Mac Low (2007a), we assume that the heating rate of the gas is

$$\Gamma_{H_2,g} = \frac{7.2 \times 10^{-12}}{(1 + n_{\text{cr}}/n_H)} \left. \frac{dn_{H_2}}{dt} \right|_{\text{form}} \text{ erg s}^{-1} \text{ cm}^{-3}, \quad (50)$$

where

$$\frac{1}{n_{\text{cr}}} = \frac{1 - 2x_{H_2}}{n_{\text{cr},H}} + \frac{2x_{H_2}}{n_{\text{cr},H_2}}, \quad (51)$$

and

$$\begin{aligned}\log n_{\text{cr,H}} &= 3.0 - 0.461T_4 - 0.327T_4^2, \\ \log n_{\text{cr,H}_2} &= 4.845 - 1.3T_4 + 1.62T_4^2,\end{aligned}\quad (52)$$

with $T_4 = T_g/10^4$ K and where the first equation, accounting for H_2 –H interactions, is an order of magnitude less than the value given by Lepp & Shull (1983), as recommended by Martin, Schwarz & Mandy (1996), and for H_2 – H_2 interactions the equation is taken from Shapiro & Kang (1987).

In addition to heating due to molecular hydrogen formation, we investigated (using calculations similar to those presented in Section 4.4) the effect of including gas heating during H_2 photodissociation and due to UV pumping of H_2 (Glover & Mac Low 2007a). However, we found that it is usually insignificant. The extra heating only has a significant effect when the gas is initially highly molecular *and* has a low metallicity ($Z \lesssim 0.1 Z_\odot$). Such circumstances are highly unrealistic because the low extinction favours prior destruction of the H_2 . Even then, the heating only affects the outer, low-density ($n_{\text{H}} \lesssim 10^3 \text{ cm}^{-3}$) parts of the clouds (because of H_2 self-shielding) which are even less likely to be molecular than the inner parts of the clouds. Since we find this heating to be insignificant in realistic situations, and for the sake of simplicity, we do not include this effect.

3 IMPLEMENTATION

The calculations presented in this paper were performed using a three-dimensional SPH code based on the original version of Benz (1990; Benz et al. 1990), but substantially modified as described in Bate, Bonnell & Price (1995), Whitehouse et al. (2005), Whitehouse & Bate (2006), Price & Bate (2007), and parallelized using both OPENMP and the message passing interface (MPI).

Gravitational forces between particles and a particle’s nearest neighbours are calculated using a binary tree. The cubic spline kernel is used and the smoothing lengths of particles are variable in time and space, set iteratively such that the smoothing length of each particle $h = 1.2(m/\rho)^{1/3}$, where m and ρ are the SPH particle’s mass and density, respectively (see Price & Monaghan 2007, for further details). The SPH equations are integrated using a second-order Runge–Kutta–Fehlberg integrator (Fehlberg 1969) with individual time steps for each particle (Bate et al. 1995). To reduce numerical shear viscosity, we use the Morris & Monaghan (1997) artificial viscosity with α_v varying between 0.1 and 1 while $\beta_v = 2\alpha_v$ (see also Price & Monaghan 2005).

3.1 Implementation of the new method

In this section, we describe the detailed implementation of the method described in Section 2. The two main new elements are the implicit integration of equations (12)–(14), and the calculation of the dust attenuation which is required to compute the local ISR that appears in equations (27), (35), and the extinction in equation (39).

3.1.1 Solving the energy equations

In solving the energy equations (12)–(14), we closely follow the implementation of the flux-limited diffusion method of Whitehouse et al. (2005) and Whitehouse & Bate (2006). The energy equations are very similar to those for the pure flux-limited diffusion method, except that the dust and gas now have different temperatures and

there are some additional heating and cooling terms. Whitehouse et al. (2005) developed an implicit method for solving equations (3) and (4) based on writing the equations in terms of the specific radiation energy, $\xi = E/\rho$, and the specific internal energy of the gas, u . For each SPH particle i , implicit expressions were derived for these two quantities at time step $n + 1$. These two equations were combined so as to solve for ξ_i^{n+1} and u_i^{n+1} . The values from the previous time step, ξ_i^n and u_i^n , were used as the initial guesses for ξ_i^{n+1} and u_i^{n+1} , and Gauss–Seidel iteration was performed over all particles that were being evolved until the quantities converged to a given tolerance. The same basic method is used here.

During each Gauss–Seidel iteration, the dust temperature must be solved for first. Equation (14) is solved directly for T_d of each particle based on its quantities from the previous time step or iteration. This is a root finding problem, for which Newton–Raphson iteration converges very quickly. It involves computing the left-hand side of equation (14) and its derivative with respect to T_d , which is straightforward except for the fact that κ_d is a function of T_d . However, since κ_d is stored in a table as a function of T_d (see Section 3.3), we simply use a numerical derivative to calculate $d(\kappa_d)/d(T_d)$.

Once the dust temperatures have been found, we solve for ξ_i^{n+1} and u_i^{n+1} in a similar manner to Whitehouse et al. (2005), but including the additional terms. However, we found it necessary to solve the equations in two different ways in the low-density and high-density regimes, reflecting the fact that equations (12)–(14) can be combined in two ways. In the low-density regime, when the gas and dust are poorly coupled, we solve

$$\begin{aligned}\rho \frac{D}{Dt} \left(\frac{E}{\rho} \right) &= -\nabla \cdot \mathbf{F} - \nabla \mathbf{v} : \mathbf{P} - a c \kappa_g \rho (T_r^4 - T_g^4) \\ &\quad + \rho \Lambda_{\text{ISR}} + \Lambda_{\text{gd}},\end{aligned}\quad (53)$$

$$\begin{aligned}\rho \frac{Du}{Dt} &= -p \nabla \cdot \mathbf{v} + a c \kappa_g \rho (T_r^4 - T_g^4) \\ &\quad - \Lambda_{\text{gd}} - \Lambda_{\text{line}} + \Gamma_{\text{cr}} + \Gamma_{\text{pe}} + \Gamma_{\text{H}_2, \text{g}},\end{aligned}\quad (54)$$

where we have obtained 53 by rearranging equation (14) to solve for the term $a c \kappa_d \rho (T_r^4 - T_d^4)$ and replaced this term in equation (12). This works well in the poorly coupled regime because the Λ_{gd} term is very small. Furthermore, in the low-density regime the gas temperature is usually $T_g \ll 1000$ K and hence $\kappa_g \approx 0$. Thus, the two equations are almost uncoupled. However, in the well-coupled regime, we find it better to solve

$$\begin{aligned}\rho \frac{D}{Dt} \left(\frac{E}{\rho} \right) &= -\nabla \cdot \mathbf{F} - \nabla \mathbf{v} : \mathbf{P} - a c \kappa_g \rho (T_r^4 - T_g^4) \\ &\quad - a c \kappa_d \rho (T_r^4 - T_d^4),\end{aligned}\quad (55)$$

$$\begin{aligned}\rho \frac{Du}{Dt} &= -p \nabla \cdot \mathbf{v} + a c \kappa_g \rho (T_r^4 - T_g^4) + a c \kappa_d \rho (T_r^4 - T_d^4) \\ &\quad + \rho \Lambda_{\text{ISR}} - \Lambda_{\text{line}} + \Gamma_{\text{cr}} + \Gamma_{\text{pe}} + \Gamma_{\text{H}_2, \text{g}},\end{aligned}\quad (56)$$

where we have obtained equation (56) by rearranging equation (14) to solve for Λ_{gd} and replaced this term in equation (13). These equations are almost identical to those solved by Whitehouse et al. (2005), except for the last four terms in equation (56), and these all tend to be very small when the gas and dust are well coupled. This form is better in the well-coupled regime because the Λ_{gd} term in equations (53) and (54) can become very large when the gas and dust are well coupled even if the difference in the gas and dust

temperatures is very small ($|T_g - T_d| \ll 0.1$ K). In this case, the Gauss–Seidel iterations can fail to converge and/or the radiation energy density can become negative. We use equations (53) and (54) when $n_{\text{H}_2}(Z/Z_\odot) < 10^{11} \text{ cm}^{-3}$ and $|T_r - T_d| > 1$ K, otherwise we use equations (55) and (56).

We solve equations (53) and (54) or equations (55) and (56) implicitly in a similar manner to Whitehouse et al. (2005). For equations (55) and (56), we write

$$\begin{aligned} \xi_i^{n+1} = & \xi_i^n + dt \sum_j \frac{m_j}{\rho_i \rho_j} bc (\rho_i \xi_i^{n+1} - \rho_j \xi_j^{n+1}) \frac{\nabla W_{ij}}{r_{ij}} \\ & - dt (\nabla v_i) f_i \xi_i^{n+1} \\ & - dt ack_{g,i} \left[\frac{\rho_i \xi_i^{n+1}}{a} - \left(\frac{u_i^{n+1}}{c_{v,i}} \right)^4 \right] \\ & - dt ack_{d,i} \left[\frac{\rho_i \xi_i^{n+1}}{a} - T_{d,i}^4 \right], \end{aligned} \quad (57)$$

where

$$b = \frac{\lambda_i}{\kappa_i \rho_i} + \frac{\lambda_j}{\kappa_j \rho_j} \quad (58)$$

for brevity, and

$$\begin{aligned} u_i^{n+1} = & u_i^n + dt (pdV_i^n) + dt ack_{g,i} \left[\frac{\rho_i \xi_i^{n+1}}{a} - \left(\frac{u_i^{n+1}}{c_{v,i}} \right)^4 \right] \\ & - 10^{-33} dt \frac{n_{\text{H}_2,i}^2}{\rho_i} T_{g,i}^{1/2} \left(\frac{u_i^{n+1}}{c_{v,i}} - T_{d,i} \right) \frac{Z}{Z_\odot} \\ & - dt \frac{\alpha_i}{\rho_i} \left(\frac{T_{g,i}}{10 \text{ K}} \right)^{\beta_i} \frac{Z}{Z_\odot} \\ & + dt \frac{\Gamma_{\text{cr},i}}{\rho_i} + dt \frac{\Gamma_{\text{pe},i}}{\rho_i} \frac{Z}{Z_\odot} + dt \frac{\Gamma_{\text{H}_2,g,i}}{\rho_i}, \end{aligned} \quad (59)$$

in which we have taken equation (36) rather than (37). The equations obtained when solving equations (53) and (54) are very similar (and simpler) to the above-mentioned equations so we omit them for the sake of brevity. Note that for an ideal gas, the temperature of the gas is given by $T_g = u/c_v$, where c_v is the specific heat capacity. In fact, our equation of state is considerably more complex (see Section 3.2) and c_v is in fact simply the ratio of u/T_g which is obtained from a pre-calculated table of values that gives this ratio as a function of u and ρ . Equation (59) includes the quantity pdV_i^n which is an explicit term (i.e. evaluated at time step n) for the work done on the gas and the thermal contribution from the artificial viscosity. In Whitehouse et al. (2005), these terms were included implicitly, but from Bate (2010) onwards we have used the explicit term here rather than the implicit term because we found empirically that using the explicit term results in better energy conservation in star formation calculations. The explicit term for particle i is calculated as

$$\begin{aligned} pdV_i = & \frac{P_i}{\Omega_i \rho_i^2} \sum_j m_j \mathbf{v}_{ij} \cdot \nabla_i W_{ij}(h_i) \\ & - \frac{1}{2} \sum_j \frac{m_j}{\rho_{ij}} \bar{\alpha}_{ij} v_{\text{sig}}(\mathbf{v}_{ij} \cdot \hat{\mathbf{r}}_{ij}) \mathbf{v}_{ij} \cdot \left[\frac{\nabla_i W_{ij}(h_i)}{2\Omega_i} + \frac{\nabla_i W_{ij}(h_j)}{2\Omega_j} \right], \end{aligned} \quad (60)$$

where the second term is only applied between approaching particles ($\mathbf{v}_{ij} \cdot \hat{\mathbf{r}}_{ij} < 0$), the viscous signal velocity is $v_{\text{sig}} = \bar{c}_s - 2v_{ij} \cdot \hat{\mathbf{r}}_{ij}$, and the average sound speed and densities of particles i and j are given by $\bar{c}_s = \frac{1}{2}(c_{s,i} + c_{s,j})$, and $\bar{\rho}_{ij} = \frac{1}{2}(\rho_i + \rho_j)$, respectively. The viscosity parameters evolve for each particle based on the method of Morris & Monaghan (1997), and their average is $\bar{\alpha}_{ij} = \frac{1}{2}(\alpha_i + \alpha_j)$.

Within each Gauss–Seidel iteration, for each particle i , equations (57) and (59) are solved simultaneously for u_i^{n+1} and then ξ_i^{n+1} . This could be done exactly for the equations used by Whitehouse et al. (2005). Note, however, that equation (59) includes the quantities $T_{g,i}^{1/2}$ and $(T_{g,i})^{\beta_i}$ in the collisional dust–gas term and the line cooling term, and the heating rate due to molecular hydrogen formation, $\Gamma_{\text{H}_2,g}$, also involves the gas temperature. For a purely implicit solution of u_i^{n+1} , the terms involving $T_{g,i}$ should be written as $T_{g,i} = u_i^{n+1}/c_{v,i}$, but this would introduce fractional powers of u_i^{n+1} , making direct solution impractical. Instead, in equation (59) we take $T_{g,i} = u_i^n/c_{v,i}$ and rely on the fact that u_i^n is updated in every Gauss–Seidel iteration so that if u_i^{n+1} converges, so too does u_i^n . Empirically, this seems to work well as long as large decreases in the gas temperature (which would result in a large decrease in the emission line cooling) are avoided from one iteration to the next – we limit $u_i^{n+1} \geq 0.8u_i^n$.

Apart from these changes, the simultaneous solution for u_i^{n+1} and then ξ_i^{n+1} follows the method of Whitehouse et al. (2005) and will not be repeated here. Briefly, in general, equations (57) and (59) are combined to eliminate ξ_i^{n+1} and produce a quartic equation for u_i^{n+1} that can be solved analytically. When solving the implicit version of equation (54) we use Newton–Raphson iteration to obtain u_i^{n+1} . Once u_i^{n+1} is obtained, ξ_i^{n+1} is found simply by rearranging equation (57). This is done for all active particles for each iteration, and the iterations are repeated until a desired tolerance is reached.

3.1.2 Calculating the ISR attenuation

It is necessary to calculate the local intensity of the ISR (attenuated due to dust extinction) and the mean visual extinction in order to evaluate the Λ_{ISR} and Γ_{pe} terms and to model the chemistry (Section 2.5). This is potentially very difficult computationally because it involves integrating over all angles at each point in the simulation. To make this computationally tractable, we use a similar method to the TREECOL method of Clark, Glover & Klessen (2012a). They propose calculating the mass surrounding a particle in angular cones (and thereby calculating the column density and optical depths) using the same tree which is frequently used in SPH codes to calculate gravity and neighbouring particles. The algorithm essentially sums over the column densities of nearby particles and more distant tree nodes that intersect the angular cone being considered. To cover the full 4π steradians uniformly, they used angular cones defined using the HEALPIX¹ library functions (Górski et al. 2005).

We implement a very similar method to that of Clark et al. (2012a), with the following differences. The SPH code used by Clark et al. used an oct-tree. An oct-tree is constructed by a purely spatial decomposition of the particle distribution and the size and shape of each node in the tree is well defined (in three dimensions, it is a cube with a size that is purely a function of its level in the tree hierarchy). This allowed Clark et al. to roughly approximate the size and shape of each node projected on to the sphere as a square, thereby allowing them to easily calculate whether or not a node contributed to the mass lying in a particular angular cone. In turn, this

¹ <http://healpix.jpl.nasa.gov/>

allowed them to construct a method that conserved the total mass (i.e. average column density). However, the SPH code we use for this paper uses a binary tree based on a nearest-neighbour decomposition (Benz et al. 1990). Thus, the nodes do not have well-defined shapes or sizes. We still implement a method that guarantees the average column density is exactly preserved, but for simplicity we assume that the projected shape of each node is a circle. Similarly, we assume that the projection of the solid angle covered by each HEALPIX direction is a circle with area $4\pi/N$ steradians, where N is the chosen number of HEALPIX directions. The binary tree defines a size for the n th node as

$$s_n = \max\left(\frac{m_2}{m_1 + m_2}r_{12} + s_1, \frac{m_1}{m_1 + m_2}r_{12} + s_2\right), \quad (61)$$

where the subscripts 1 and 2 identify the two subnodes, $r_{ij} = |\mathbf{r}_i - \mathbf{r}_j|$, and m_i and \mathbf{r}_i are the mass and position of the centre of mass of the subnodes, respectively. If the subnode is an individual SPH particle, its size is zero in equation (61). As mentioned above, in general the tree nodes do not have well-defined shapes. For the purposes of calculating the column density, we assume their projection is circular, but we are free to scale their effective radius by an arbitrary factor so that the radius of the circle is $r_n = fs_n$, where f is expected to be of order unity. We explore the effects of choosing different values of f in Section 4.1 and conclude that $f = 0.5$ is a good choice. If the node is an individual SPH particle, we take the radius to be twice the particle's smoothing length, $r_n = 2h_n$. From a particular particle, p , at location, \mathbf{r}_p , the vector between the particle and the node is $\mathbf{r}_{np} = \mathbf{r}_n - \mathbf{r}_p$. We then define the angular radius of the node as viewed from the particle by $a_n = \arctan(r_n/r_{np})$. We denote the HEALPIX direction as $\hat{\mathbf{l}}$, which we treat as the centre of the HEALPIX circle of angular radius $a_{\text{pix}} = \sqrt{4/N}$ (the π s cancel). The angular distance between the centres of these two circles is $d = \arccos(\mathbf{r}_{np} \cdot \hat{\mathbf{l}}/r_{np})$.

To calculate the contribution of each tree node or particle to the column density in each HEALPIX area, we calculate the overlapping area of the two circles. For two circles of radii r and R whose centres are separated by distance d , this can be computed as

$$\begin{aligned} A &= r^2 \arccos\left(\frac{d^2 + r^2 - R^2}{2dr}\right) \\ &+ R^2 \arccos\left(\frac{d^2 + R^2 - r^2}{2dR}\right) \\ &- \frac{1}{2} \sqrt{(-d+r+R)(d+r-R)(d-r+R)(d+r+R)}, \end{aligned} \quad (62)$$

where we take $r = a_{\text{pix}}$ and $R = a_n$. The contribution of the node to the average column density of the HEALPIX area is then $m_n/(\pi r_n^2)A/(4\pi/N)$, where $m_n/(\pi r_n^2)$ is the column density of the node and $A/(4\pi/N)$ is the fraction that is assigned to that HEALPIX area. The computational efficiency can be improved by treating trivial cases separately. If $a_n + a_{\text{pix}} \leq d$, there is no overlap. If $d + a_{\text{pix}} \leq a_n$, then the HEALPIX area is entirely covered by the node and the contribution is simply $m_n/(\pi r_n^2)$. If $d + a_n \leq a_{\text{pix}}$, then the node lies entirely within the HEALPIX area and the contribution is $m_n/(4\pi/N)$.

Once we have determined the average column density in a particular HEALPIX area, we can calculate the visual extinction A_V in that direction. We define $Q_V = Q_V(V)$ at a visual wavelength of 550 nm. Rather than performing the integrals appearing in equations (27) and (35) during an SPH calculation, we pre-calculate tables of values.

For equation (35), the attenuated dust heating in a single direction as a function of $\log(A_V)$

$$\lambda^{\text{ISR}}(A_V) = \int_0^\infty Q_V J_V^{\text{ISR}} \exp\left[-\frac{A_V}{1.086} \frac{Q_V(v)}{Q_V}\right] dv, \quad (63)$$

where the factor of 1.086 = 2.5 log(e) appears because extinction A is related to optical depth τ by $A = -2.5 \log(e^{-\tau})$. The integral is actually calculated in $d(\ln v)$ rather than dv . This table can be interpolated to find the heating rate for any particular value of the visual extinction A_V . The total heating rate at a location is then provided by averaging the contributions from all directions $\hat{\mathbf{l}}_i$ as

$$\Lambda_{\text{ISR}} = \frac{1}{N} \sum_i^N \lambda^{\text{ISR}}(A_{V_i}), \quad (64)$$

where the directions are chosen using the HEALPIX library functions. The same is done to compute the quantity $G(\mathbf{r})$ for the photoelectric heating (equation 27). We pre-calculate a table of values along a single line of sight containing

$$g(A_V) = \frac{\int_{6\text{eV}}^\infty J_V^{\text{ISR}} \exp\left[-\frac{A_V}{1.086} \frac{Q_V(v)}{Q_V}\right] dv}{\int_{6\text{eV}}^\infty J_V^{\text{ISR}} dv}. \quad (65)$$

The total value $G(\mathbf{r})$ at a location (equation 27) is then provided by averaging the contributions from all directions $\hat{\mathbf{l}}_i$ as

$$G(\mathbf{r}) = \frac{1}{N} \sum_i^N g(A_{V_i}). \quad (66)$$

For equations (39) and (46), we simply have

$$\langle \exp(-A_V) \rangle = \frac{1}{N} \sum_i^N \exp(-A_{V_i}). \quad (67)$$

To calculate the average column density of molecular hydrogen $\langle N_{\text{H}_2} \rangle$ which is required to evaluate the self-shielding of molecular hydrogen (equation 47), we use the same traversal of the tree that is used to calculate the extinction and $G(\mathbf{r})$, but rather than calculate the full column density the contribution of each particle or tree node is multiplied by its molecular fraction x_{H_2} .

It should be noted that even using the same tree that is used to calculate gravitational forces to estimate the extinction and other directional averages, obtaining the averages in many directions can still require a substantial amount of computation. Furthermore, when the code is run in parallel using MPI with domain decomposition, the contributions of each domain to the column densities along each ray must be added together in order to calculate the quantities in each direction. This would not be necessary if one simply wanted the average column density to a particle (since the column density adds linearly), but because calculating the extinction involves a non-linear function, $\exp(-\tau)$, the column density in each direction must be computed separately. Thus, when running with MPI domain decomposition there is also a substantial memory overhead which depends on the chosen number of directions.

3.2 Equation of state and boundary conditions

As in Bate (2009, 2012), the calculations presented in this paper were performed using RHD with an ideal gas equation of state for the gas pressure $p = \rho T_g \mathcal{R}/\mu$. The thermal evolution takes into account the translational, rotational, and vibrational degrees of freedom of molecular hydrogen (assuming a 3:1 mix of ortho- and

para-hydrogen; see Boley et al. (2007). It also includes molecular hydrogen dissociation, and the ionizations of hydrogen and helium. The hydrogen and helium mass fractions are $X = 0.70$ and $Y = 0.28$, respectively. For this composition, the mean molecular weight of the gas is initially $\mu = 2.38$. The contribution of metals to the equation of state is neglected.

In previous calculations using the flux-limited diffusion method of Whitehouse et al. (2005), it was necessary to set matter and radiation temperature boundary conditions. For calculations contained within a particular volume (e.g. the collapse of a molecular cloud core; Whitehouse & Bate 2006; Bate 2010, 2011; Bate, Tricco & Price 2014), the matter and radiation temperatures were fixed on ghost particles outside the boundary at the initial (low) temperature (e.g. 10 K). For calculations of clouds with free boundaries (e.g. Bate 2009, 2012, 2014), all particles with densities less than a particular value (typically 10^{-21} g cm⁻³) had their matter and radiation temperatures set to the initial values (again ≈ 10 K). This matter was two orders of magnitude less dense than that in the initial cloud and, thus, these boundary particles surrounded the region of interest in which the star cluster formed. In both cases, this essentially meant that the clouds were embedded in an external radiation field with this boundary temperature.

The new method presented here eliminates the need for these arbitrary temperature boundary conditions. Now the temperature of the gas, dust and radiation are all set consistently at both high and low densities.

3.3 Opacities and metallicity

Whitehouse & Bate (2006), Bate (2009, 2010, 2011, 2012), and Bate et al. (2014) assumed solar metallicity gas and used the Rosseland mean opacity tables of Pollack, McKay & Christofferson (1985) for interstellar dust and, at higher temperatures when the dust is destroyed, the gas opacity tables of Alexander (1975, the IVa King model); see Whitehouse & Bate (2006) for further details. Bate (2014) performed calculations with varying opacities. He used the same dust opacities, scaled linearly in proportion to the metallicity, but replaced the gas opacity tables with the metallicity-dependent tables of Ferguson et al. (2005) with $X = 0.70$. It is worth noting that one of the main conclusions of Bate (2014) was that the results of star formation calculations are very insensitive to the opacities that are used.

In this paper, because the equations treating dust heating and photoelectric heating of the gas require integrals over the dust opacity as a function of frequency, we cannot continue simply to use the Rosseland mean opacities of Pollack et al. (1985). At low-densities (i.e. when the optical depth is low and the dust is essentially in thermal equilibrium with the ISR field), the Planck mean is more appropriate than the Rosseland mean, and we desire consistency between the frequency-dependent dust opacity, $Q_v(\nu)$ and the grey opacity, κ_d , appearing in equations (12) and (14). In other words, equation (15) should be satisfied. Therefore, we calculate Planck mean opacities directly from $Q_v(\nu)$ before the code begins to evolve the SPH calculation and the values are stored in a table as a function of dust temperature. Any frequency dependent opacities can be used in principle, but for simplicity, we use the parametrization provided by Zucconi et al. (2001) of the opacities from Ossenkopf & Henning (1994). We use these values for κ_d whenever the dust temperature is less than 100 K. We assume that higher dust temperatures ($T_d > 100$ K) will only be encountered at high densities (i.e. near protostars) when the gas and dust are optically thick and thermally well-coupled. In this case, Rosseland mean opacities are

appropriate, and we use those of Pollack et al. (1985) as we have in our earlier calculations mentioned above.

For the gas, we continue to use the Rosseland mean opacities of Ferguson et al. (2005) for κ_g , since the gas opacity only becomes important in the highly optically-thick regions inside, or very near to, a star, for which the Rosseland mean is appropriate.

4 CALCULATIONS

4.1 Testing the method for calculating ISR attenuation

One of the tests that Clark et al. (2012a) used for the TREECOL method was to calculate the temperature structure of two uniform-density spherical clouds when subjected to a Black (1994) ISR field. They took densities of 10^{-19} g cm⁻³ for clouds with masses of 1 and 10 M_\odot and used 2.6×10^5 SPH particles. We perform the same tests here. For this test, we set the internal radiation to zero (i.e. $E = T_r = 0$) and we turn off the coupling between the gas and the dust (i.e. $\Lambda_{gd} = 0$) so that equation (14) is only solving for the equilibrium temperature of the dust subject to the attenuated external ISR. The ISR is as discussed in Section 2.4.1, except that we exclude the additional UV flux which is important for photoelectric heating. We have calculated the exact radial temperature distribution by analytically calculating the column density along 192 HEALPIX directions (using 48 provides an almost identical result) and used these values to calculate the attenuated dust heating (equations 63 and 64) and the equilibrium dust temperature as functions of radius.

In Fig. 2, we give the distribution of the equilibrium dust temperature as a function of radius for each of the two clouds. One point is plotted for each SPH particle. Different colours give the results obtained when the code uses 12, 48, or 192 HEALPIX directions to calculate the mean extinction. The number of HEALPIX directions used has little impact on the results, except in the very outer part of the clouds when using only 12 directions. However, using more directions takes longer to compute, so from this point on we use 48 HEALPIX directions. The equilibrium temperature of dust that is subject to the full ISR is 17.2 K for our chosen ISR. By considering equation (23), we expect a dust particle that is subject to one hemisphere of heating to have an equilibrium temperature that is a factor of $2^{1/6}$ lower (i.e. 15.3 K) and, as expected, this is essentially equal to the temperature at the edge of each of the clouds. However, within the clouds we find that the dust temperatures are up to ≈ 1 K warmer than given by the exact solutions (solid black lines). We note that the central temperatures in our clouds are in good agreement with those found by Clark et al. (2012a), but they obtained substantially lower temperatures at the outer edges of their clouds (13–14 K). The reason for this is not clear since, as just mentioned, our edge temperatures are what we would expect. Their ISR may have been different to ours, although both are nominally based on that of Black (1994).

In Fig. 3, we plot the dust temperatures from five calculations of the 1- M_\odot cloud that each use 48 HEALPIX directions, but that have different numbers of SPH particles: 280, 2608, 2.6×10^4 , 2.6×10^5 , and 2.6 million. It can be seen that the dust temperature tends to be overestimated when a smaller number of particles is used, but the dust temperature appears to be slowly converging towards the exact solution as the number of particles is increased. The error in the dust temperature is approximately halved each time the number of SPH particles is increased by an order of magnitude (i.e. the error decreases at about the same rate that the linear spatial resolution increases). Comparing the 2.6×10^4 particle calculation with the exact solution, the maximum difference between the mean

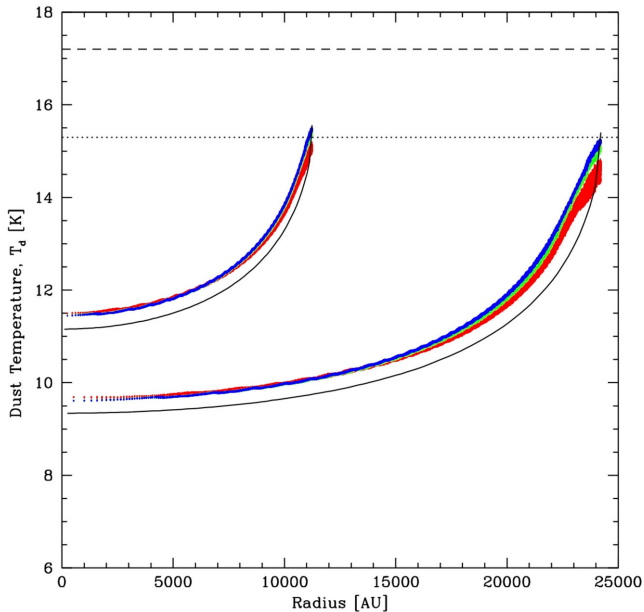


Figure 2. The dust temperature as a function of radius inside two uniform-density molecular cloud cores that are subject to an external ISR field. The clouds have the same densities, but different masses: $1 M_{\odot}$ (upper distributions) and $10 M_{\odot}$ (lower distributions). The exact solutions are plotted using the solid black lines. For the SPH calculations, a point is plotted for each SPH particle (2.6×10^5 for each cloud). The different colours give the results obtained when the code uses 12 (red), 48 (green), or 192 (blue) HEALPIX directions to calculate the mean extinction. Dust within the clouds receives less of the external radiation due to extinction and, therefore, is colder. The number of HEALPIX directions used has little impact on the results, except in the very outer part of the clouds. The equilibrium temperature of dust that is subject to the full ISR is 17.2 K (horizontal dashed line), and the equilibrium temperature of dust that received exactly half of this radiation would be 15.3 K, which is lower by a factor of $2^{1/6}$ (horizontal dotted line). As expected, dust at the edges of the clouds is close to this temperature.

temperatures at any radius is only 1 K. Clark et al. (2012a) did not discuss how their method behaves with different numbers of particles.

We used a cubic lattice SPH particle distribution to generate the results presented in Figs 2 and 3. We have also tried a random particle distribution. Using 2.6×10^5 randomly-placed SPH particles to model the $1-M_{\odot}$ cloud, we obtained an almost identical mean radial temperature distribution to the case that used a cubic lattice, but with a temperature scatter of up to ± 0.2 K. However, given that this error is similar to the systematic difference between the temperature distributions obtained from the 2.6×10^5 and 2.6 million particle cubic lattice calculations, we conclude that the accuracy of the solution depends more on the number of particles used than on the details of how they are distributed.

In Fig. 4, we investigate the effects on the calculation of the dust temperature of varying the tree-opening criterion and the effective radius of the tree nodes, the latter of which is parametrized by the factor f (see Section 3.1.2). During the walk through the tree to calculate gravity, nodes are opened if s_n/r_{np} is larger than a critical value, usually taken to be 0.5. We perform calculations using a tree-opening parameter of 0.5 and 0.25 (the latter of which means more nodes are opened during the tree walk). For each case, we perform five SPH calculations of the $1-M_{\odot}$ cloud that each use 48 HEALPIX directions and 2.6×10^5 SPH particles, but we vary the effective

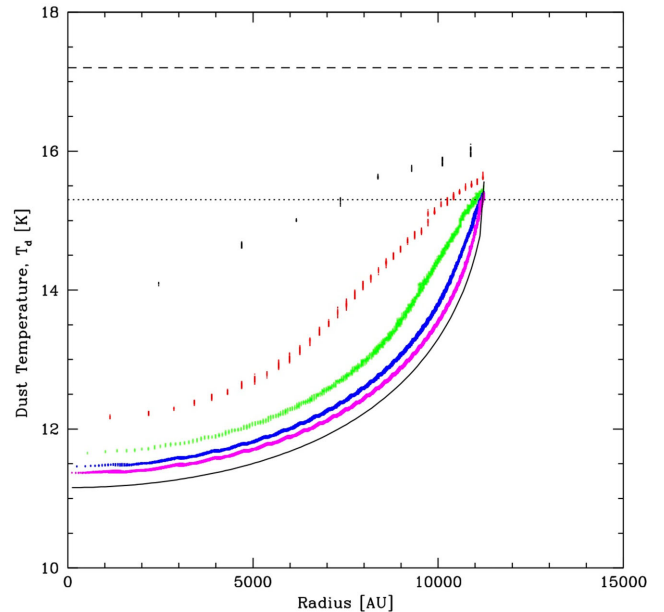


Figure 3. The dust temperature as a function of radius inside the $1 M_{\odot}$ uniform-density molecular cloud core that is subject to external ISR. The exact solution is plotted using the solid black line. The results from five SPH calculations are illustrated, and a point is plotted for each SPH particle. The calculations each use 48 HEALPIX directions to calculate the mean extinction, but different numbers of SPH particles are used to model the cloud – from top to bottom: 280 (black), 2608 (red), 2.6×10^4 (green), 2.6×10^5 (blue), and 2.6 million (magenta). It can be seen that using fewer particles tends to result in warmer dust temperatures (i.e. an underestimate of the extinction), but the dust temperature appears to be slowly converging towards the exact solution as the number of particles is increased. As long as $\gtrsim 3 \times 10^4$ particles are used the maximum error in the mean temperature at any radius is $\lesssim 1$ K. The equilibrium temperature of dust that is subject to the full ISR is 17.2 K (horizontal dashed line), and the equilibrium temperature of dust that received exactly half of this radiation would be 15.3 K, which is lower by a factor of $2^{1/6}$ (horizontal dotted line). As expected, with sufficient resolution, the dust at the edges of the clouds is close to this temperature.

radius of the node that is used when calculating the column density. We take factors of $f = 2.0, 1.0, 0.5, 0.1,$ and 0.01 . It can be seen from Fig. 4 that using very large tree-opening angles and/or effective node radii results in warmer dust temperatures (i.e. an underestimate of the extinction). We also note that almost identical results are obtained when the product of the opening parameter and the factor f is a constant (e.g. using a tree-opening parameter of 0.5 and $f = 1$ gives almost identical results to using a tree-opening parameter of 0.25 and $f = 2$). The calculation of the extinction becomes very poor when the product of these two quantities exceeds ≈ 0.5 . If the effective node size is too small, the calculations provide reasonable mean temperatures at a given radius, but the scatter increases (e.g. the black points in the left-hand panel that were produced using $f = 0.01$). With the typical tree-opening parameter of 0.5, setting the factor $f = 0.5$ gives the best trade-off between accurately computing the mean radial temperature distribution and minimizing the scatter.

The typical resolutions employed in SPH calculations of star cluster formation vary from $\sim 10^3$ particles per solar mass (Bonnell, Bate & Vine 2003; Bonnell et al. 2011) to $\sim 10^5$ particles per solar mass (Bate, Bonnell & Bromm 2003; Bate 2012). The results of this test suggest that the typical errors in the dust temperature due to finite numbers of SPH particles and HEALPIX directions and variations

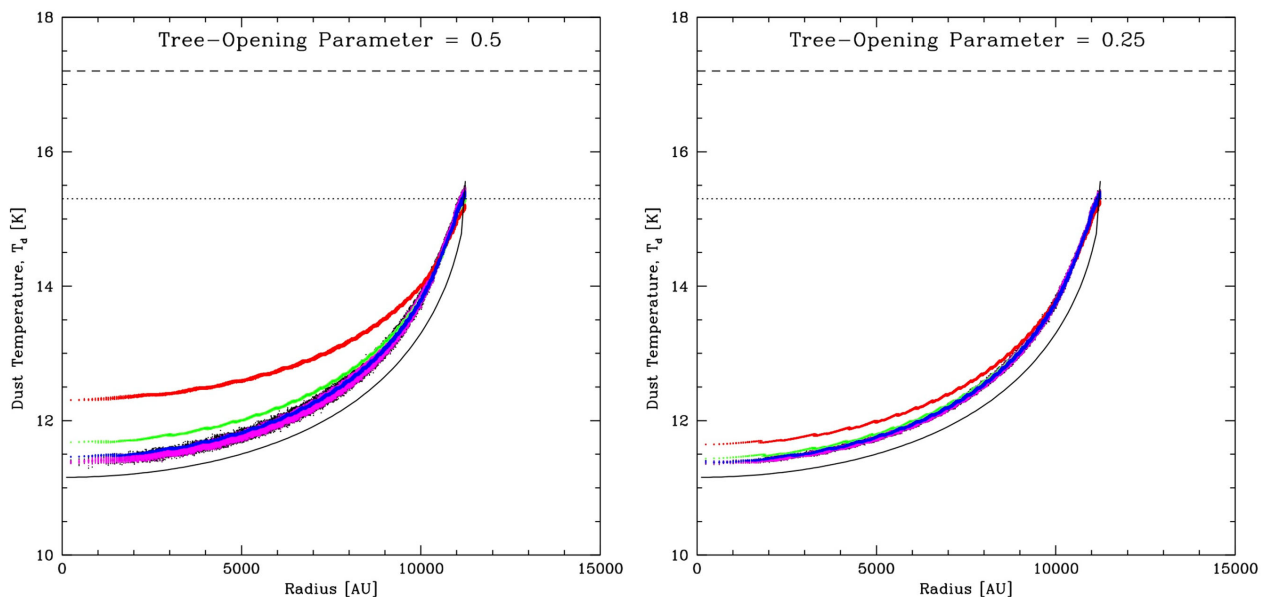


Figure 4. The dust temperature as a function of radius inside the $1 M_{\odot}$ uniform-density molecular cloud core that is subject to external ISR. The exact solution is plotted using the solid black line. The results from 10 SPH calculations are illustrated, and a point is plotted for each SPH particle. The calculations each use 48 HEALPIX directions to calculate the mean extinction and 2.6×10^5 SPH particles, but the tree-opening parameter and the effective sizes of the tree nodes are varied. In the left-hand panel, the tree-opening parameter is 0.5, while in the right-hand panel it is 0.25. In each panel, the effective size of the tree nodes decreases from top to bottom, using scaling factors of $f = 2.0$ (red), 1.0 (green), 0.5 (blue), 0.1 (magenta), and 0.01 (black). It can be seen that using very large tree-opening angles and/or effective node sizes results in warmer dust temperatures (i.e. an underestimate of the extinction). If the effective node size is too small, the scatter increases. With a tree-opening parameter of 0.5, an effective node size of half the actual node size (i.e. $f = 0.5$) gives the best trade-off between accurately computing the mean radial temperature distribution and minimizing the scatter. The equilibrium temperature of dust that is subject to the full ISR is 17.2 K (horizontal dashed line), and the equilibrium temperature of dust that received exactly half of this radiation would be 15.3 K, which is lower by a factor of $2^{1/6}$ (horizontal dotted line). As expected the dust right at the edges of the clouds is close to this temperature.

of the tree parameters should be $\lesssim 1$ K as long as $\gtrsim 3 \times 10^4$ particles per solar mass are used and large effective node radii are avoided.

4.2 Equilibrium dust and gas temperatures

More realistic than using a uniform-density sphere is to use Bonner–Ebert spheres. To allow comparison with earlier work, we use the same $5-M_{\odot}$ Bonner–Ebert spheres that were used by Keto & Field (2005) – a (marginally) subcritical case with a central density of $n_{\text{H}_2} = 10^4 \text{ cm}^{-3}$, and a supercritical case with a central density of $n_{\text{H}_2} = 10^6 \text{ cm}^{-3}$. The former case has a ratio of the inner to outer density of 14, while the ratio of the latter is 3000. Their radii are 0.223 and 0.265 pc, respectively. In these tests, we assume the hydrogen is fully molecular. We model both clouds with 3×10^5 SPH particles.

The SPH particles were set up using a cubic lattice which was then deformed radially to obtain the required cumulative radial mass profile. In Fig. 5, we provide the SPH density as a function of radius for of each SPH particle for both cores. The small ‘spikes’ in the density in the supercritical case are due to the lattice structure affecting the density calculation of some particles in this case with a very strong density gradient. They do not appear in the subcritical case, which has a much shallower density profile. In both cases, there is also some ‘noise’ in the density near the outer boundary (which is made of reflected ghost particles).

In this section, we investigate the effects of each of the physical heating and cooling mechanisms on the temperatures of the gas and dust. We begin by including only cosmic ray heating and molecular line cooling for the gas, and the dust is taken to be in thermal

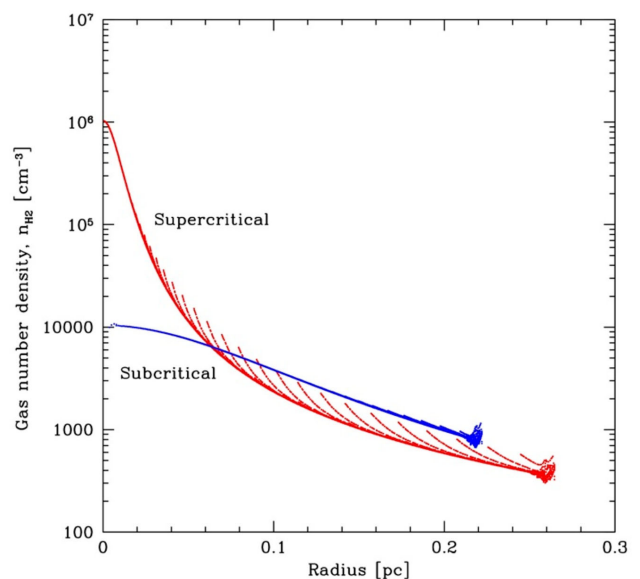


Figure 5. Plots of the SPH molecular hydrogen number density, n_{H_2} , as functions of radius inside the subcritical (blue) and supercritical (red) $5-M_{\odot}$ Bonner–Ebert spheres. A point is plotted for each SPH particle. The ‘spikes’ in the density for the supercritical case are an artefact of the particles being set up on a radially-deformed cubic lattice.

equilibrium with the ISR. We then add in the effects of gas–dust collisions, photoelectric heating of the gas and cooling from C^+ . For the first two cases, we also investigate the effects of including and excluding the UV flux.

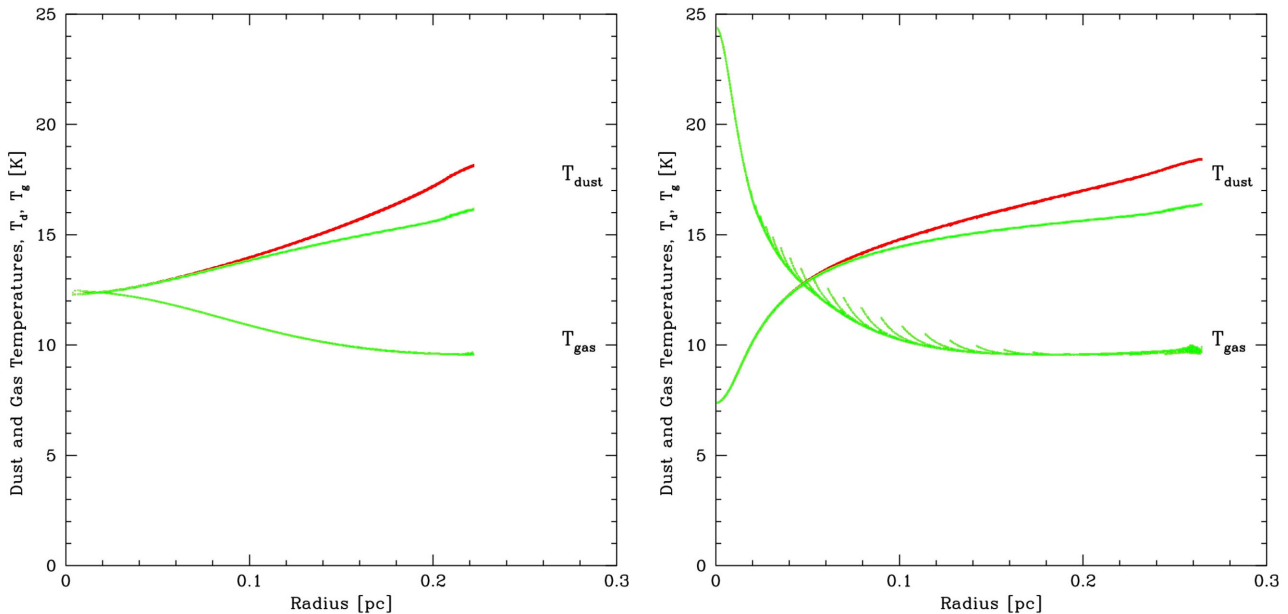


Figure 6. The dust (upper) and gas (lower) temperatures as functions of radius inside the subcritical (left) and supercritical (right) $5\text{-}M_{\odot}$ Bonner–Ebert spheres. The ISM physics includes cosmic ray heating and molecular line cooling of the gas, and the dust is in thermal equilibrium with an external ISR that excludes (green) or includes (red) the UV contribution (see Section 2.4.1). The dust temperature drops as the extinction increases at smaller radii. The gas temperature rises because the line cooling becomes less effective at higher densities. The UV ISR only affects the dust temperature in the low-extinction outer parts of the cloud. The small ‘spikes’ in the gas temperature in the right plot at radii $r \approx 0.03\text{--}0.16$ pc are due to the artefacts in the calculation of the SPH density due to the particles being set up on a radially-perturbed cubic lattice.

4.2.1 Cosmic ray heating, molecular line cooling, and dust radiative equilibrium

In Fig. 6, we plot the dust and gas temperatures as functions of radius inside the two Bonner–Ebert spheres. These calculations include only cosmic ray heating and undepleted molecular line cooling of the gas, and the dust is in thermal equilibrium with the external ISR. There is no gas–dust collisional coupling, photoelectric effect, or cooling due to C^+ , oxygen, or recombination lines. There are two calculations for each case – one that excludes the UV contribution to the ISR, and one that includes it.

In the outer parts of the cores, the dust temperature exceeds the gas temperature as the local ISR is only weakly attenuated by the dust, and the cosmic ray flux and line cooling are such that the low-density equilibrium gas temperature is ≈ 10 K. Including the UV contribution to the ISR boosts the dust temperature by up to 2 K in the outer parts, but the total energy in the UV flux is small compared to the total ISR flux and the UV does not penetrate very far into the cores. In the inner parts of the cores, the gas temperature rises as the effectiveness of the line cooling decreases (Goldsmith 2001). On the other hand, the dust temperature decreases, particularly in the supercritical case, because the dust extinction attenuates the ISR.

4.2.2 The effects of gas–dust collisions

In Fig. 7, we include the same physical processes as in the previous section, but we now also turn on the transfer of thermal energy between the gas and the dust due to collisions. The strength of this interaction depends on the square of the density (equation 36), so we expect it to have little impact at low densities, but a significant impact as the density increases. Indeed, this can be clearly seen in Fig. 7, in which we plot the same calculations as in Fig. 6 for reference, but we now also include the case with gas–dust coupling

in blue (without the UV ISR) and magenta (with the UV ISR). The gas–dust thermal coupling has no significant effect on the temperatures in the subcritical core because the densities are too low. In the supercritical case, the dust temperature is unaffected, but the gas temperature at $r < 0.04$ pc (densities $n_{\text{H}_2} \gtrsim 2 \times 10^4$) is ‘dragged down’ by the interaction with the cold dust so that at the centre the gas and dust temperatures are both ≈ 7.5 K.

Our numerical results are in reasonable agreement with those presented in figs 4 and 5 of Keto & Field (2005), who use the same models for the ISM physics as we use here, without the UV ISR (black solid lines in Fig. 7). The main difference is that the gas temperatures at low densities are slightly lower in Keto & Field (2005). The gas temperature at low density is set by the balance between cosmic ray heating and the line cooling rates. The latter is dependent on the method used to interpolate from the tables of Goldsmith (2001). Since the cosmic ray heating and line cooling rates are both simple functions of n_{H} (equations 24 and 34), it is easy to solve for the central gas temperature of 12.4 K in the subcritical case (where the gas–dust coupling is negligible). The slightly lower gas temperature (≈ 11.5 K) obtained by Keto & Field (2005) was found to be due to less accurate interpolation used by Keto & Field of the line cooling functions of Goldsmith (2001). Thus, the different interpolation of the line cooling produces the different gas temperatures.

4.2.3 The effects of photoelectric heating and carbon chemistry

In Fig. 8, in addition to the other physical processes, we turn on photoelectric heating of the gas due to UV ISR photons liberating electrons from dust grains (equation 26). The resulting gas and dust temperatures (green) are compared to those without the photoelectric heating (blue). The dust temperature is essentially unchanged, but the gas temperature in the outer parts of the cores, at densities

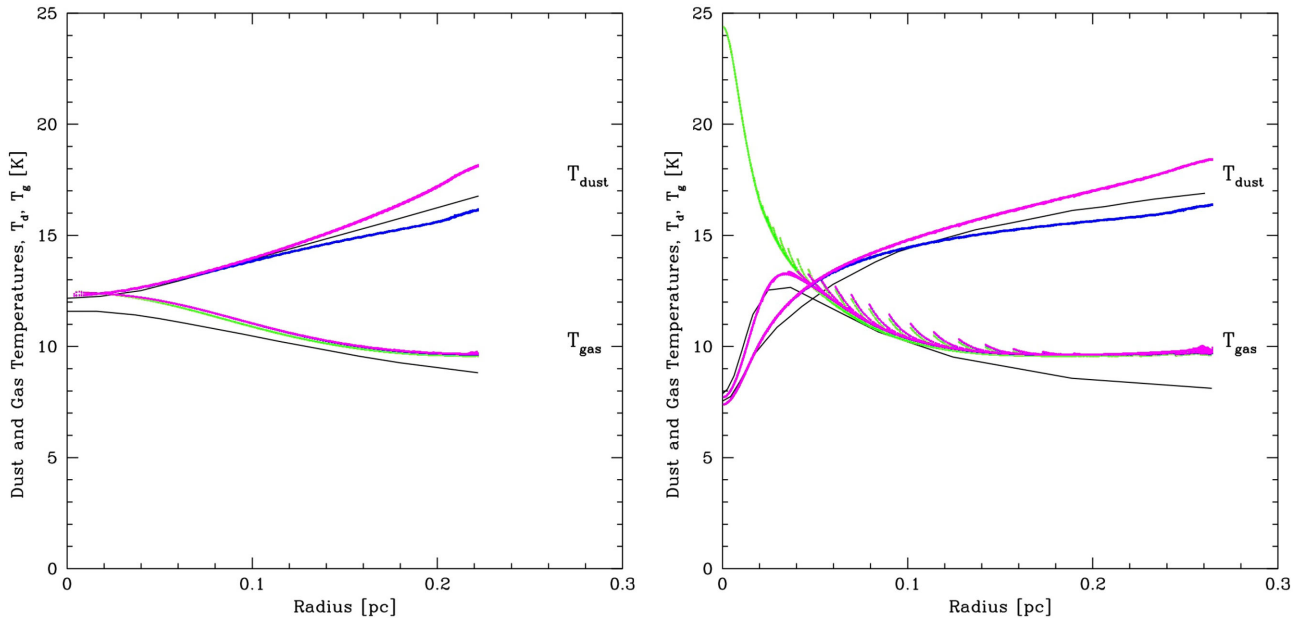


Figure 7. The dust (upper) and gas (lower) temperatures as functions of radius inside the subcritical (left) and supercritical (right) $5\text{-}M_{\odot}$ Bonner–Ebert spheres. Red and green points (mostly obscured) are the same as in Fig. 6. For the blue (without the UV ISR) and magenta (with the UV ISR) points, the ISM physics is exactly the same, except that it includes thermal collisional coupling between the gas and the dust. The black solid lines give the results obtained by Keto & Field (2005) without including the UV ISR. The effect is that at high densities, the gas essentially adopts the dust temperature. The small ‘spikes’ in the gas temperature in the right-hand plot at radii $r \approx 0.03\text{--}0.16$ pc are due to the artefacts in the calculation of the SPH density due to the particles being set up on a radially-perturbed cubic lattice.

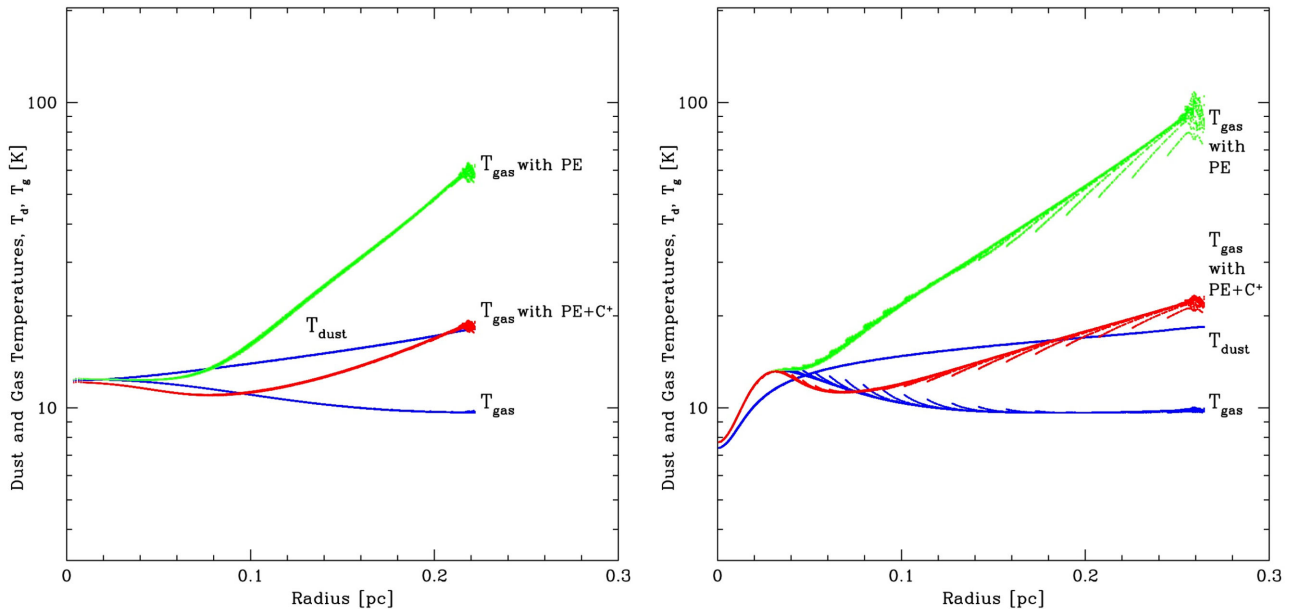


Figure 8. The effect of photoelectric heating and C^+ cooling of the gas on the dust and gas temperatures as functions of radius inside the subcritical (left) and supercritical (right) $5\text{-}M_{\odot}$ Bonner–Ebert spheres. The dust temperatures are essentially unaffected by the extra gas heating and cooling processes. The blue points are the same as in Fig. 7, where the gas is subject to cosmic ray heating, molecular line emission, and collisions with the dust, while the dust is subject to heating from the ISR (including the UV), thermal emission, and collisions with the gas. The green points include the same physical effects as the blue points, but with the addition of photoelectric gas heating (equation 26). The photoelectric heating has an enormous effect on the gas temperature in the outer, low-density parts of the clouds. However, when the C^+ cooling is included (red points), the effect of the photoelectric heating on the gas temperature is greatly reduced.

such that the gas and dust are thermally decoupled ($n_{\text{H}_2} \lesssim 10^4 \text{ cm}^{-3}$), is much hotter than without photoelectric heating. In fact the photoelectric heating is so strong that the cosmic ray heating is irrelevant in the low-density gas.

Whereas Keto & Field (2005) did not consider photoelectric heating, as discussed in Section 2.5, Keto & Caselli (2008) included photoelectric heating and a simple carbon chemistry model which allowed them to include both cooling from C^+ at low densities and

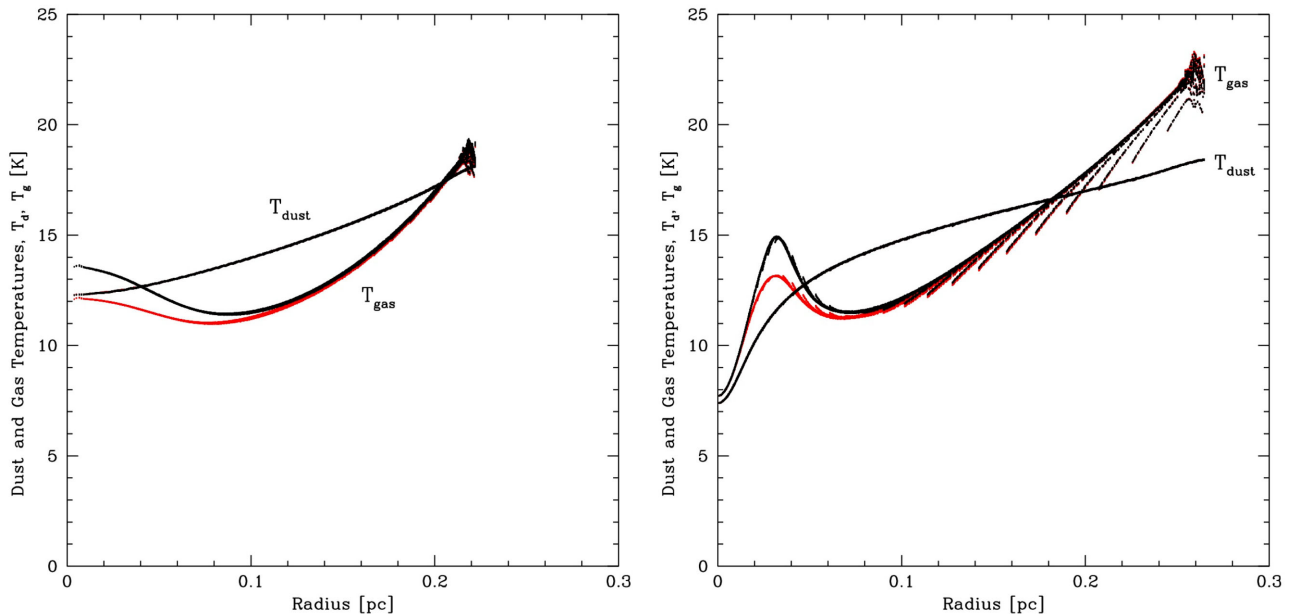


Figure 9. The effect of CO depletion on the gas on the dust and gas temperatures as functions of radius inside the subcritical (left) and supercritical (right) $5\text{-}M_{\odot}$ Bonner–Ebert spheres. The red points are the same as in Fig. 8, where the gas is subject to cosmic ray and photoelectric heating, molecular and C^+ line emission, and collisions with the dust, while the dust is subject to heating from the ISR (including the UV), thermal emission, and collisions with the gas. The black points include the same physical processes as the red points, but also allow for CO depletion. This reduces the molecular line cooling at high densities which raises the gas temperature slightly at densities $n_{\text{H}_2} = 10^4\text{--}10^5\text{ cm}^{-3}$. At higher densities the depletion has little effect because the cooling is dominated by dust emission through collisions with the dust.

treat the depletion of CO at high densities. Therefore, in Fig. 8, we keep the photoelectric heating on, but also add cooling from C^+ (red). It can be seen that the C^+ cooling dramatically lowers the temperatures in the outer parts of the cloud; the temperature is still somewhat higher than it was without either the photoelectric heating or the C^+ cooling, but much less than if C^+ cooling is omitted. We note that recombination and oxygen cooling are both insignificant at these densities and that the temperatures are essentially identical whether they are included or not.

Finally, in Fig. 9 we turn on the effects of CO depletion based on the equilibrium prescription of Keto & Caselli (2008). This results in only slightly higher gas temperatures at intermediate densities ($n_{\text{H}_2} = 10^4\text{--}10^5\text{ cm}^{-3}$) where the densities are still too low for dust cooling to dominate, but the densities are high enough that C^+ is ineffective.

4.2.4 The effects of changing the ISM parameters

The previous sections used the diffuse ISM model parameters described in Sections 2.3 and 2.4. In this section, we investigate the dependence of the gas and dust temperatures on the strengths of the various external heating sources. We only use the supercritical Bonner–Ebert sphere in these tests because this has the larger range of densities. In the left-hand panel of Fig. 10, we explore the effects of changing the cosmic ray heating rate (equation 24) by an order of magnitude in each direction. In the right-hand panel of Fig. 10, we explore the effects of change the gas photoelectric heating rate (equation 26) by an order of magnitude in each direction. It can be seen that over particular density ranges, either of these changes the gas temperature by approximately half an order of magnitude in each direction because the gas line cooling scales roughly

as the square of the gas temperature for the molecular lines (Goldsmith 2001). The gas temperatures in the outer parts of the cloud are much more strongly affected by photoelectric heating than cosmic ray heating. On the other hand, at number densities $n_{\text{H}_2} \gtrsim 10^5\text{ cm}^{-3}$ strong cosmic ray heating can raise the gas temperature significantly above the dust temperature whereas the photoelectric heating has no effect this deep within the core.

In Fig. 11, we probe the effects of changing the ISR field (equation 25) by an order of magnitude in each direction, excluding the UV contribution which is held fixed. The calculations include photoelectric heating of the gas and C^+ cooling. The increased ISR primarily affects the dust temperature, but because the dust emission scales as the sixth power of its temperature (equation 23), this only has a 50 percent effect on the dust temperatures. Deep within the core where the gas becomes thermally coupled to the dust, the warmer or cooler dust also results in warmer or cooler gas, respectively.

In Fig. 12, we investigate the effects of changing the metallicity of the core, performing additional calculations with metallicities of 1 percent, 10 percent, and 3 times solar. It can be seen that the highest metallicity results in the coldest temperatures for both the gas and the dust due to the combination of several effects. The increased metallicity increases the ISR attenuation, decreasing the dust temperature inside the core. Similarly, the UV is prevented from penetrating as far into the core, reducing the effects of photoelectric heating of the gas, and the gas line emission is enhanced. Finally, there is an increase in the effectiveness of collisional thermal coupling between the gas and the dust. With the lowest metallicity, the dust almost becomes isothermal since there is almost no attenuation of the ISR, and the gas is warmer because the photoelectric heating is strong while emission line cooling is weak.

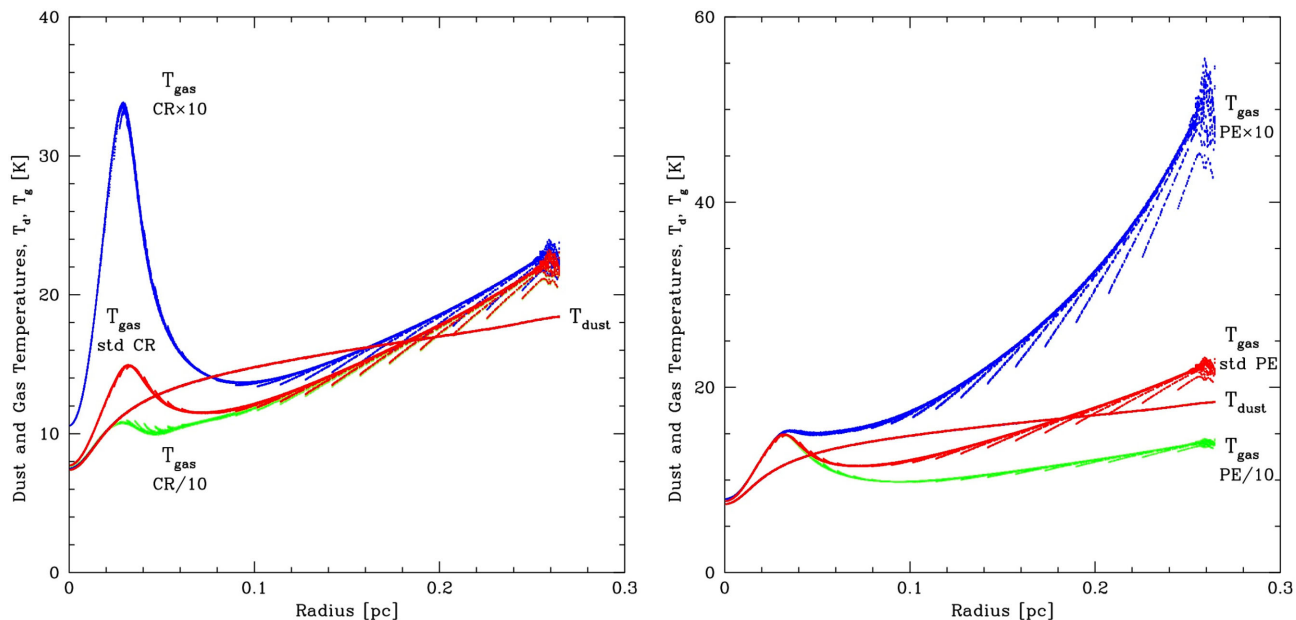


Figure 10. The effects of changing the strengths of the cosmic ray (left) and photoelectric (right) heating of the gas on the dust and gas temperatures as functions of radius inside the supercritical $5\text{-}M_{\odot}$ Bonner–Ebert sphere. In both panels, the red points are the same as in the black points in the right-hand panel of Fig. 9. The other points include the same physical effects as the red points, but with one order of magnitude less (green) or more (blue) cosmic ray (left) or photoelectric (right) heating. Changing the level of cosmic ray heating has a large effect on the gas temperature at intermediate densities, but not at high densities (where the gas and dust are well coupled) or low densities (where photoelectric heating dominates). Changing the levels of photoelectric heating has a large effect on the gas temperature only in the outer regions of the core. The dust temperatures are unaffected in either case.

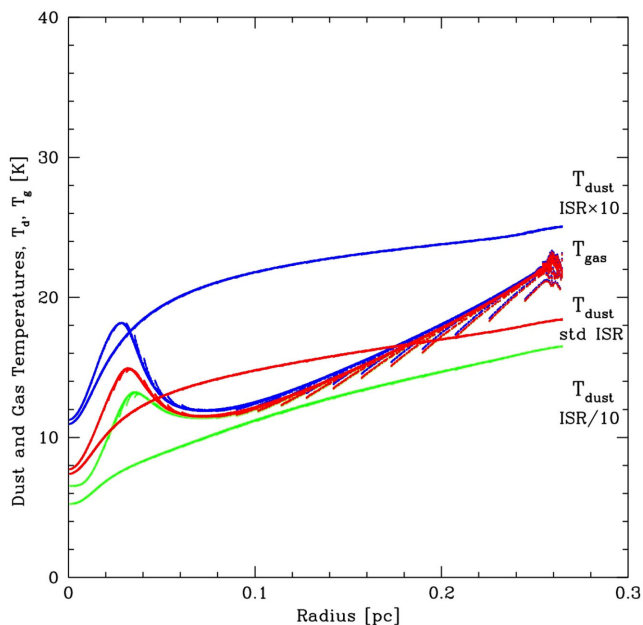


Figure 11. The effects of changing the strength of the ISR field on the dust and gas temperatures as functions of radius inside the supercritical $5\text{-}M_{\odot}$ Bonner–Ebert sphere. The red points are the same as the black points in the right-hand panel of Fig. 9. The other points include the same physical effects as the red points, but with one order of magnitude less (green) or more (blue) ISR heating. Changing the level of ISR by an order of magnitude has a 50 per cent effect ($10^{1/6}$) on the dust temperatures. At high densities, the different dust temperature affects the gas temperature in a similar manner, but at low densities the gas temperature is unaffected as it is set by the photoelectric heating and C^+ cooling.

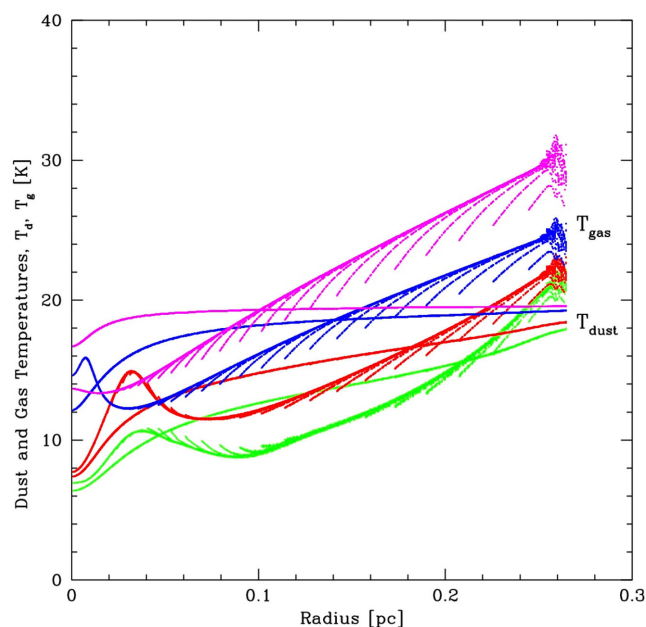


Figure 12. The effects of changing the metallicity on the dust and gas temperatures as functions of radius inside the supercritical $5\text{-}M_{\odot}$ Bonner–Ebert sphere. Photoelectric heating has been included. From top to bottom, the calculations have metallicities of 1/100 (magenta points, top curves), 1/10 (blue points), solar metallicity (red points), and 3 times solar metallicity (green points). The red points are the same as in the black points in the right-hand panel of Fig. 9. The dust temperatures are greater with lower metallicities because the ISR is less attenuated by extinction. The gas temperatures are greater with lower metallicities because the UV ISR is less attenuated by extinction (leading to stronger photoelectric heating) and also because the gas emission line cooling is reduced.

4.3 The evolution of a collapsing Bonner–Ebert sphere

In this section, as opposed to the static tests from the previous sections, we report the results from a hydrodynamical calculation of the collapse of a Bonner–Ebert sphere and compare them to the results obtained using the pure flux-limited diffusion method of Whitehouse et al. (2005) and Whitehouse & Bate (2006). We begin with a somewhat unstable Bonner–Ebert sphere, similar to those studied in the previous section. We choose a $5\text{-}M_{\odot}$ core with an inner to outer density contrast of 20 and a radius of 0.1 pc. We model the core with 3×10^5 SPH particles and use spherical reflective boundary conditions (modelled using ghost particles).

In Fig. 13, we plot the central temperatures as functions of the central (maximum) density for the two methods. All of the initial temperatures in the pure flux-limited diffusion calculations are arbitrary. As is standard practice in such calculations, we set the matter and radiation temperatures to be in thermal equilibrium initially. We perform two separate calculations and with two different initial temperatures of 10 and 14 K. For the calculation performed using the method described in this paper, the initial gas and dust temperatures are not arbitrary – they are set by our model of the diffuse ISM. The initial dust temperature increases from 8 K in the centre to 17 K at the outer edge of the molecular cloud core. The initial gas temperature is slightly warmer than the dust at the centre (10 K) and cooler at the outside (≈ 15 K). The initial central dust and gas temperatures are quite similar because the central density of the core is quite high ($\rho = 6 \times 10^{-19} \text{ g cm}^{-3}$ or $n_{\text{H}_2} = 1.5 \times 10^5 \text{ cm}^{-3}$) so that there is significant thermal coupling between the dust and the gas (we use equation 36 in these calculations). As the collapse

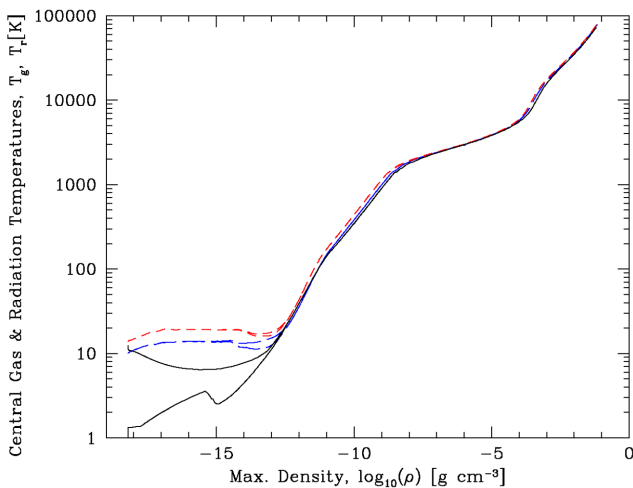


Figure 13. The evolution of the central gas and radiation temperatures as functions of the maximum (central) density during a radiation hydrodynamical calculation of the collapse of an unstable spherical $5\text{-}M_{\odot}$ Bonner–Ebert sphere. The radiation temperature is always less than or equal to the gas temperature in this graph. After the central density exceeds $10^{-17} \text{ g cm}^{-3}$, the central dust temperature is indistinguishable from that of the gas. The black solid lines give the results from a calculation using the method described in this paper, while the red dashed lines and blue long-dashed lines give the results using the pure FLD method of Whitehouse & Bate (2006). The diffuse ISM model used in the former calculation determines the initial gas and dust temperatures, which vary with radius, and the internal radiation temperature is arbitrarily set to a low initial value (1 K). In the FLD calculations, the initial temperatures of the matter (gas and dust) and internal radiation are arbitrary and we set them to 14 K (red dashed) and 10 K (blue long-dashed). As expected, it is mainly the low-density evolution that is affected by including the diffuse ISM model.

proceeds, the central dust and gas temperatures quickly converge, so we do not plot the central dust temperature in Fig. 13. The increases in extinction and density during the collapse mean that both the dust and gas temperatures drop to a minimum of 6.5 K when the central density is $10^{-16} \text{ g cm}^{-3}$ before the compressional heating starts to increase the central temperature again. The initial radiation temperature should be set to a low value, because the heating of the initial conditions is via external radiation rather than internal radiation. As long as a small value is chosen the exact value is unimportant, but we wish to avoid setting it to zero so as to avoid numerical problems. We chose a value of 1 K.

As may be expected, Fig. 13 shows that it is mainly the low-density phase of evolution of the clouds that differs between the two methods (densities $\lesssim 10^{-13} \text{ g cm}^{-3}$). Once the central regions of the core become optically-thick to infrared radiation (the so-called opacity limit for fragmentation; Low & Lynden-Bell 1976; Rees 1976) all of the temperatures converge. The evolution obtained with the pure flux-limited diffusion calculation with the lower initial temperature (10 K) is closest to the evolution obtained using the method presented here, presumably because the central temperature in this model is closest to that given by the ISM initial conditions.

In Fig. 14, we plot temperature profiles as functions of radius (left-hand panel) and density (right-hand panel) at various points during the collapse. Gas is shown with solid lines, dust with dotted lines, and radiation with dashed lines. At either a given radius or density the temperatures tend to rise during the collapse as the protostar emits more radiation. The formation of the stellar core at late times (initial radius $\approx 0.01 \text{ au}$ and temperature $> 10^4 \text{ K}$) is clearly visible in the left-hand panel. Except in the outer parts of the core, these profiles are very similar to those obtained using pure flux-limited diffusion. The main difference in the outer parts of the core (radii $\gtrsim 10^3 \text{ au}$) is that the gas, dust, and radiation all have different temperatures with the new method, whereas with pure flux-limited diffusion all are very close to the initial arbitrary temperature (e.g. 10 K; see Whitehouse & Bate 2006).

After stellar core formation as radiation works its way outwards from the centre the gas, dust, and radiation temperatures become inverted at intermediate radii in the core (radii 400–3000 au; Fig. 15). Before this point the gas temperature is the hottest and the radiation temperature the coldest at these radii. However, the radiation emitted by the protostar quickly dominates that from the external radiation field at these radii. The dust adopts a new thermodynamic equilibrium with the combined radiation field, being heated to temperatures of 15–40 K, but the gas which is poorly coupled to either the radiation or the dust at these low densities remains at temperatures of 8–12 K. Such effects are impossible to capture unless the thermal evolution of the gas and dust are treated separately.

4.4 The evolution of an isolated turbulent molecular cloud

Glover & Clark (2012a,c) studied the thermodynamics of turbulent molecular clouds with different metallicities. In particular, they performed calculations of $10^4 M_{\odot}$ clouds, typically modelled using SPH with 2 million particles. Their initial conditions consisted of a uniform-density sphere of number density $n_{\text{H}} = 300 \text{ cm}^{-3}$, giving a radius of approximately 6 pc. The cloud was given initial ‘turbulent’ motions with a power spectrum $P(k) \propto k^{-4}$, where k is the wavenumber. The energy in the turbulence was initially set equal to the magnitude of the gravitational potential energy of the cloud, giving an initial root-mean-square velocity of around 3 km s^{-1} . The turbulence was allowed to decay freely. The calculations were performed using a confining pressure of $p_{\text{ext}} = 1.2 \times 10^4 \text{ K cm}^{-3}$

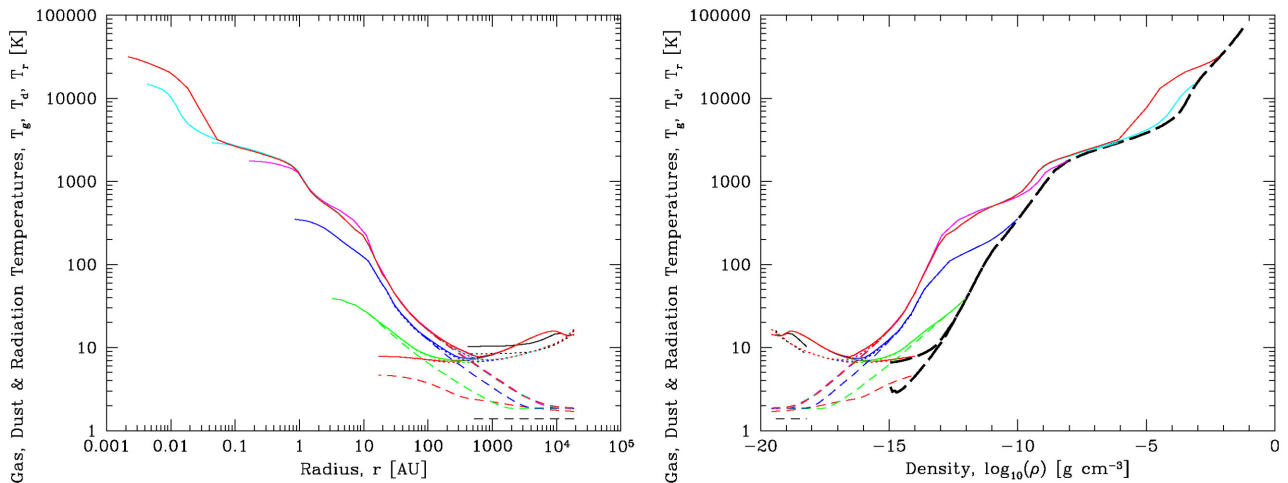


Figure 14. The evolution of the gas (solid), dust (dotted), and radiation (dashed) temperatures as functions of radius (left-hand panel) and maximum density (right-hand panel) during a radiation hydrodynamical calculation of the collapse of an unstable spherical $5\text{-}M_{\odot}$ Bonner–Ebert sphere. Each colour gives the state of the calculation when the maximum density reaches a different value, with the initial conditions given in black. The radiation temperature is always less than or equal to the gas temperature in this graph. The thick black long-dashed lines in the right-hand panel give the evolution of the central gas and radiation temperatures with central density from Fig. 13 for reference (only for $\rho > 10^{-15} \text{ g cm}^{-3}$). It can be seen that for a given density the gas is usually hotter later in the collapse than earlier due to radiation from the protostar heating the outer parts of the core. The formation of the stellar core is apparent in the upper-left of the left-hand panel (initial radius $\approx 0.01 \text{ au}$).

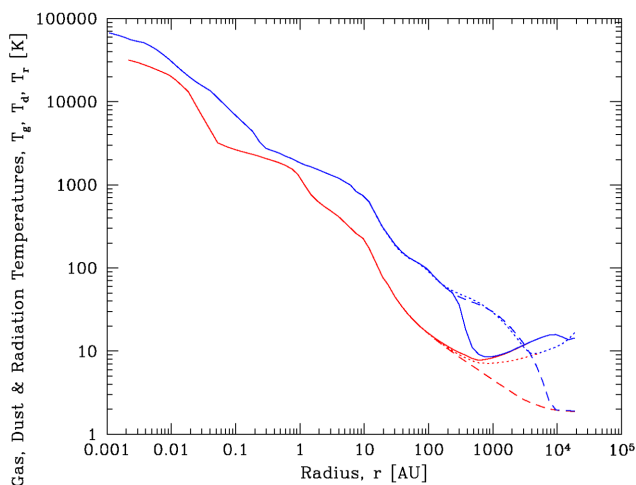


Figure 15. The gas (solid), dust (dotted), and radiation (dashed) temperatures as functions of radius when the collapsing spherical $5\text{-}M_{\odot}$ Bonner–Ebert sphere has reached a maximum density of 0.01 g cm^{-3} (lower, red lines), and 1.76 years later at the end of the calculation when the maximum density is 0.06 g cm^{-3} (upper, blue lines). Near the end of the calculation, after the stellar core forms, the radiation and dust temperatures become hotter than the gas temperature at radii of 400–3000 au because of the radiation emitted by the protostar.

which was implemented in the SPH equations by subtracting the external pressure from the pressure used in the momentum equation. We use the same set up as Glover & Clark, although of course we are unable to use exactly the same initial velocity field. We use our full diffuse ISM model to obtain the results below, but we begin by excluding the hydrogen chemistry and heating due to the formation of molecular hydrogen (Section 2.5.2). In the first set of results, we have also excluded molecular depletion (because Glover & Clark did not include depletion), but since we find that switching depletion on or off has little effect on the results it is included in most of the subsequent calculations. For the dust–gas thermal coupling, we

switch to equation (37) because this is the equation Glover & Clark used.

4.4.1 Results excluding hydrogen chemistry

In Fig. 16, we plot the gas (upper panel) and dust (lower panel) temperatures as functions of the number density of hydrogen nuclei, n_{H} , for a calculation performed at solar metallicity. The snapshot is taken just before the first sink particle is formed. The colours in the gas temperature plot indicate the average CO abundance of each point in temperature–density space. This is the equivalent of fig. 2 in Glover & Clark (2012a) or the upper-right panel of Fig. 4 in Glover & Clark (2012c). Since Glover & Clark did not include molecular depletion on to grains, we have turned this off in our calculation. The distribution of gas temperatures with density shows the same general features seen in the papers of Glover & Clark. At low densities ($n_{\text{H}} \lesssim 10^3 \text{ cm}^{-3}$), the gas temperature rises towards $\sim 100 \text{ K}$ as the number density decreases towards $n_{\text{H}} \sim 10 \text{ cm}^{-3}$. The temperatures at densities $n_{\text{H}} \lesssim 100 \text{ cm}^{-3}$ are primarily determined by the models of photoelectric heating, and cooling due to electron recombination and emission from ionized oxygen and carbon (equations 26 to 33). The gas temperatures lie beneath the equilibrium curve (solid black line from Fig. 1) because the equilibrium curve assumes no extinction whereas in fact the photoelectric heating is generally attenuated by the dust extinction (depending on the location of the gas). Our maximum temperatures in this density regime are somewhat cooler than those obtained by Glover & Clark due to our slightly different models in this regime as already demonstrated in Fig. 1. At densities $n_{\text{H}} \approx 100\text{--}10^4 \text{ cm}^{-3}$, there is a large dispersion in the gas temperatures with a range of $T_{\text{g}} \approx 8\text{--}50 \text{ K}$ obtained at densities $n_{\text{H}} \approx 10^3\text{--}10^4 \text{ cm}^{-3}$. In this region, although there is still significant photoelectric heating, the low-density coolants just mentioned become ineffective. Instead, the main cooling is from molecular lines, in particular CO (e.g. Goldsmith 2001; Glover & Clark 2012a), which depends strongly both on density and temperature. At the same time, work from the gas motions becomes important (either

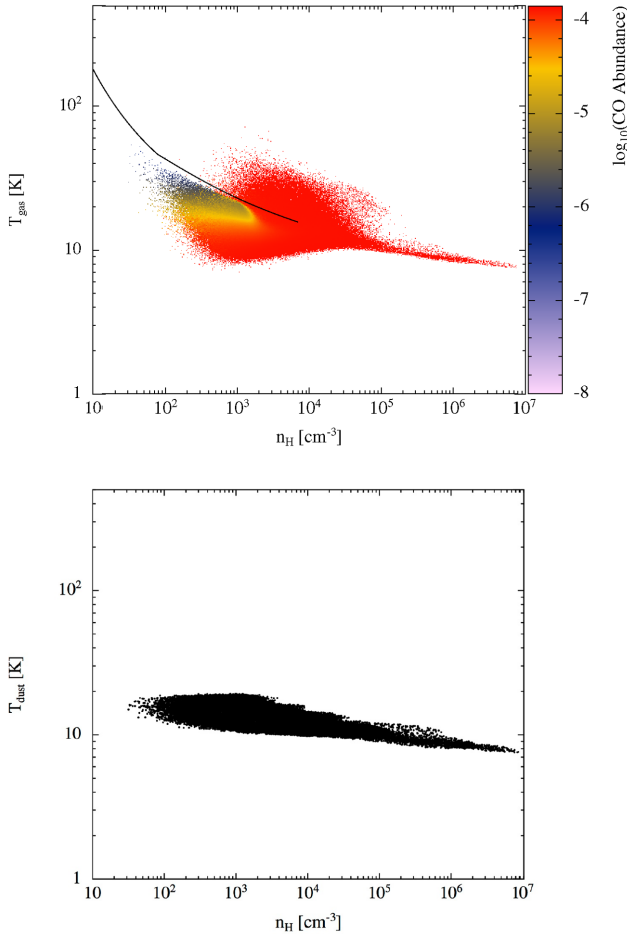


Figure 16. Phase diagrams showing the gas (top panel) and dust (lower panel) temperatures as functions of the gas density. The colours in the gas temperature plot indicate the average CO abundance of each point in temperature–density space. The black solid line in the gas temperature plot is the equilibrium curve from Fig. 1.

heating or cooling the gas, depending on whether the gas is being compressed or expanding, respectively), as does heating in shocks. Together these effects lead to the wide range in temperatures. Finally, at densities $n_{\text{H}} \gtrsim 10^5 \text{ cm}^{-3}$ thermal coupling of the gas to the dust becomes important and the gas temperature converges towards that of the dust as the density increases.

As mentioned above, Glover & Clark (2012a) do not treat depletion of CO on to dust grains. Turning this on has little effect on the phase diagram (Fig. 17). As may be expected, the temperatures at densities of $n_{\text{H}} \approx 10^3\text{--}10^5 \text{ cm}^{-3}$ are slightly higher, but the effect is hardly noticeable. At lower densities the CO is not depleted and the dominant coolant is C^+ rather than CO anyway. At higher densities where the CO does become depleted, the dominant coolant is dust.

We now explore the sensitivity of the results to several of the assumptions in our model. We examine the dependence on changes of the chemistry, in particular the abundance of C^+ and the depletion of molecules like CO on to grains, as well as the effects of variations in the molecular line cooling rates and the strength of the coupling between the gas and the dust.

The main effect of the carbon chemistry model described in Section 2.5.1 is to provide the abundances of the coolants C^+ at low-densities and CO at high densities. Typically, the transition between the dominance of the two coolants occurs at $n_{\text{H}} \sim 10^3 \text{ cm}^{-3}$ (e.g.

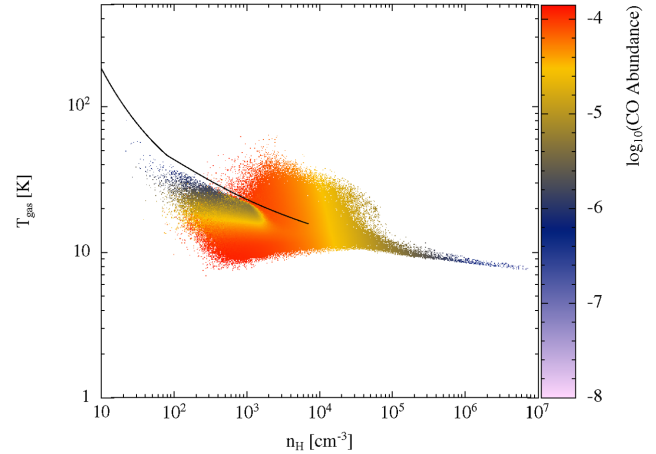


Figure 17. Phase diagram showing the gas temperature as a function of the gas density for a calculation that is identical to that portrayed in Fig. 16, except that molecular depletion is turned on. The black solid line is the equilibrium curve from Fig. 1.

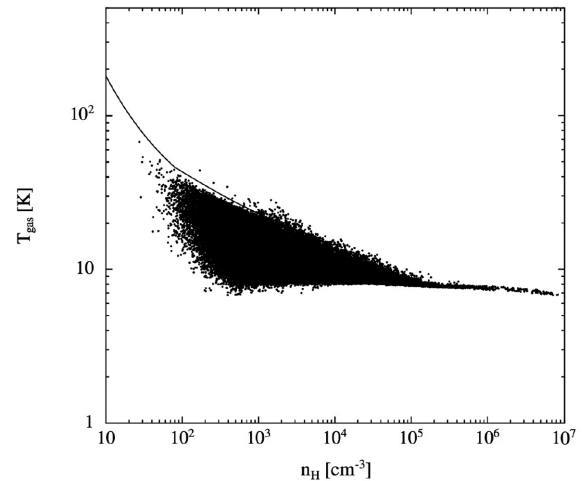


Figure 18. Phase diagram showing the gas temperature as a function of the gas density for a calculation that is identical to that portrayed in Fig. 17, except that all the carbon is assumed to be in the form of C^+ . The black solid line is the equilibrium curve from Fig. 1.

Glover & Clark 2012a). The temperature of the gas is quite sensitive to this transition from C^+ to CO. For example, in Fig. 18 we give the results obtained by assuming that the carbon remains as C^+ at all densities and we turn off all molecular cooling. In this case, essentially all of the gas lies at temperatures below the equilibrium curve of Fig. 1 and there is little gas with temperatures greater than 20 K with densities $n_{\text{H}} \approx 10^3\text{--}10^5 \text{ cm}^{-3}$. This extreme case shows that it is important to have at least a simple model that switches the carbon from C^+ to CO.

In Fig. 19, we return to our standard model including molecular depletion, but we increase the molecular line cooling rates by an arbitrary factor of 3. As expected, this decreases the temperatures of the gas with densities $n_{\text{H}} \approx 10^3\text{--}10^5 \text{ cm}^{-3}$. The lowest temperature (at densities $n_{\text{H}} \approx 10^3 \text{ cm}^{-3}$) decrease from $T_{\text{g}} \approx 8$ to ≈ 5 K, but the highest temperatures (at densities $n_{\text{H}} \approx 10^3 \text{ cm}^{-3}$) are not significantly affected.

As mentioned in Section 2.4.3, equations (36) and (37) for the gas–dust thermal coupling coefficient differ by a factor of 15 (the

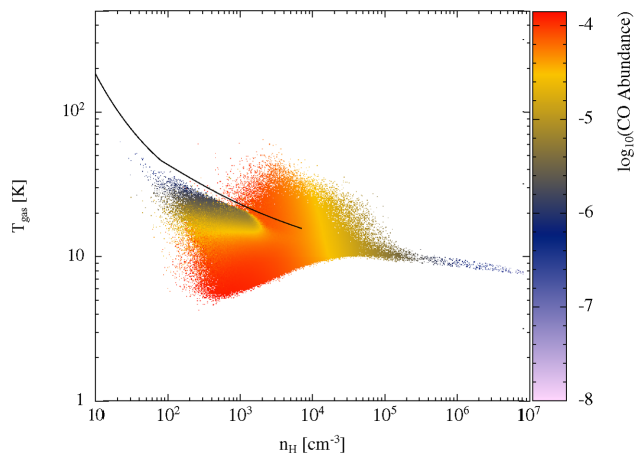


Figure 19. Phase diagram showing the gas temperature as a function of the gas density for a calculation that is identical to that portrayed in Fig. 17, except that the molecular line cooling rate has been increased by a factor of 3. The colours in the gas temperature plot indicate the CO abundance of each point in temperature–density space. The black solid line is the equilibrium curve from Fig. 1.

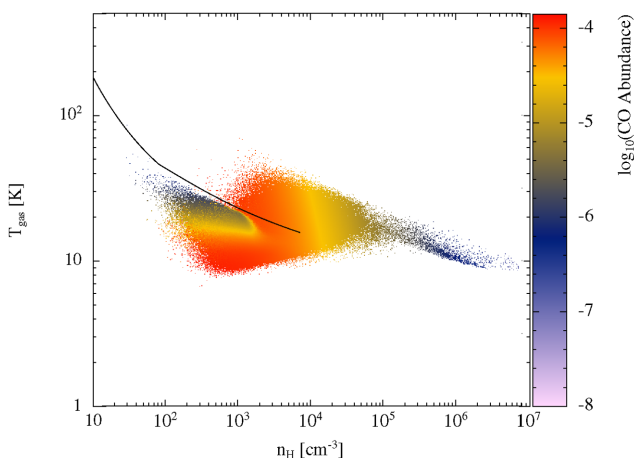


Figure 20. Phase diagram showing the gas temperature as a function of the gas density for a calculation that is identical to that portrayed in Fig. 17, except that the collisional thermal coupling between the dust and the gas is 15 times smaller (equation 36 has been used rather than 37). Note that there is a larger dispersion in the gas temperatures at densities $n_H \gtrsim 10^5 \text{ cm}^{-3}$. The black solid line is the equilibrium curve from Fig. 1.

latter, used by Glover & Clark, gives stronger coupling). Therefore, in Fig. 20 we examine the effect of using the weaker coupling provided by equation (36) instead. As expected, this only has an effect on the temperatures at high densities, $n_H \gtrsim 10^5 \text{ cm}^{-3}$. The gas shows a somewhat increased spread of temperatures because the coupling with the dust is not strong enough to force the gas to adopt the dust temperature.

In summary, the gas temperatures in solar metallicity turbulent clouds are relatively independent of many of the parameters of our diffuse ISM model. The most important factors are the low-density equilibrium model (portrayed in Fig. 1) which essentially sets an upper limit to the temperatures at densities $n_H \lesssim 10^3 \text{ cm}^{-3}$, and the way in which the carbon transitions from C^+ to CO. The exact molecular cooling rates, molecular depletion, and dust–gas thermal coupling parameters are less important.

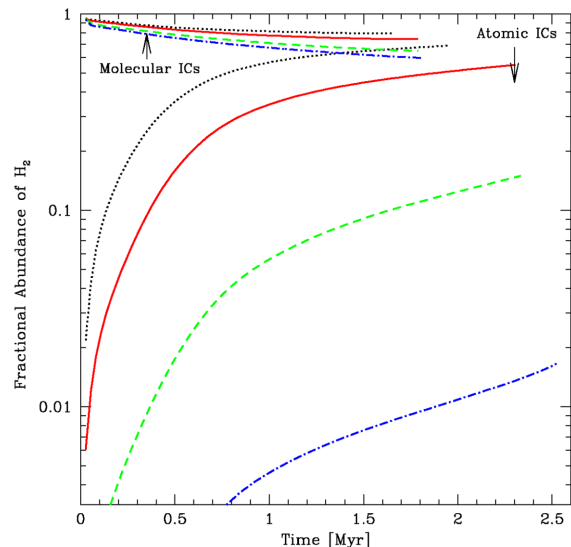


Figure 21. We plot the evolution of the total fractional abundance of molecular hydrogen in calculations of turbulent clouds up until the time that stars begin to form. For each metallicity, we perform two calculations: one with fully molecular initial conditions (upper lines) and one with fully atomic initial conditions (lower lines). The metallicities are 3 times solar (black dotted lines), solar (red solid lines), 1/10 solar (green dashed lines), and 1/100 solar (blue dot–dashed lines). By the time stars begin to form, clouds with solar or supersolar metallicity are mostly molecular, regardless of their initial H_2 abundance, but little molecular gas has formed in the low-metallicity clouds that consist of fully atomic hydrogen initially.

4.4.2 The effects of metallicity and hydrogen chemistry

Following Glover & Clark (2012c), we examine the dependence on metallicity and on hydrogen chemistry. We perform full calculations (i.e. including the simple carbon chemical model and molecular depletion) for four different metallicities: 3, 1, 1/10, and 1/100 times the solar value. For each metallicity, we perform calculations that exclude hydrogen chemistry and its associated heating terms (results from the solar metallicity case have already been displayed in Fig. 17). We also perform calculations that include the evolution of hydrogen (i.e. its molecular fraction x_{H_2}) and heating due to H_2 formation on dust grains. Two calculations are performed for each metallicity: one beginning with fully atomic hydrogen, and one beginning with fully molecular hydrogen.

In Fig. 21, we plot the evolution of the fractional abundance of molecular hydrogen in the eight calculations that include hydrogen chemistry up until the formation of the first sink particle in each calculation. This is the equivalent of fig. 3 in Glover & Clark (2012c). Beginning with fully molecular hydrogen, the decrease in H_2 is primarily due to photodissociation in the outer parts of the clouds. The destruction is greater at lower metallicities because the UV radiation is less attenuated by dust. Beginning with fully atomic hydrogen, H_2 is formed on dust grains and the total abundance monotonically increases in each calculation. However, the rate of increase strongly depends on the metallicity. The main reason for this is that there are more dust grains on which to produce H_2 at higher metallicity (equation 40) so the rate of formation is higher. In addition, the extra dust attenuates the UV radiation that destroys H_2 so the destruction rate is also lower. By the time stars begin to form, clouds with solar metallicity or higher are mostly molecular regardless of whether atomic or molecular initial conditions were adopted (particularly in the central regions where the stars actually

form). However, at lower metallicities the initial conditions matter much more. When stars begin to form in the $1/10Z_{\odot}$ calculations, the H_2 abundance is 65 per cent when beginning with molecular initial conditions, but only 15 per cent beginning with atomic initial conditions. For $1/100Z_{\odot}$, the disparity is even stronger, with the two abundances being 60 and 1.7 per cent, respectively.

The behaviour of the molecular hydrogen evolution is qualitatively similar to that reported by Glover & Clark (2012c). In particular, the growth rate of molecular hydrogen in the atomic solar-metallicity calculation matches theirs to within 10 per cent, and the decay rates of the abundances in all of the molecular calculations are very similar. The clouds in Glover & Clark (2012c) take longer to begin forming stars (2.7–4.0 Myr rather than 1.7–2.6 Myr). This difference is most likely due to the different initial turbulent velocity field. With fully molecular initial conditions, because the stars take longer to form in the calculations of Glover & Clark (2012c), the H_2 abundances when the star formation takes place are lower. This is most important in the lowest metallicity case, where the total abundance is only ≈ 20 per cent when the star formation begins in the Glover & Clark (2012c) calculation, whereas it is 60 per cent in our calculation. There are also differences in the abundances of molecular hydrogen in the lower metallicity calculations with atomic initial conditions. The total H_2 abundances when beginning with fully atomic hydrogen remain low throughout both our calculations and those of Glover & Clark. However, at any particular time our abundance is twice that obtained by Glover & Clark (2012c) with $1/10Z_{\odot}$ and it is about an order of magnitude higher for the $1/100Z_{\odot}$ case until shortly before stars begin to form (when the abundances in both calculations are ≈ 1 per cent). No doubt some of this difference is due to the different velocity field and dust opacities used in the calculations, though it is not clear whether or not this explains all of the discrepancy.

Turning to the phase diagrams of gas temperature in Fig. 22, the general trends are again in agreement with those found by Glover & Clark (2012c). First, we consider the calculations that exclude hydrogen chemistry (they assume all hydrogen is in molecular form) and its associated heating (left-hand column of Fig. 22). Increasing the metallicity above solar results in a reduction of the lower envelope of the gas temperatures at densities $n_H = 10^2$ – 10^4 cm^{-3} because the additional molecular cooling and increased extinction produces lower gas temperatures. The upper temperature envelope is less affected. Lowering the metallicity to $1/10$ of solar results in a smaller range of temperatures because extinction has less of an effect at low and intermediate densities so the temperatures tend to lie close to the equilibrium curve of Fig. 1 (which does not depend significantly on metallicity because the photoelectric heating and the cooling due to electron recombination and fine-structure emission are all assumed to be proportional to the metallicity). At higher densities, the main heating sources (compressional heating and cosmic ray heating) are independent of the metallicity and although the gas is less well coupled to the dust it is still coupled well enough that the gas temperatures are kept around 10 K. As the metallicity is reduced still further to $1/100$ solar, the temperatures move above the solar metallicity equilibrium curve of Fig. 1. This is because the cosmic ray heating (which is taken to be independent of metallicity) becomes as important as the photoelectric heating at low metallicity. Furthermore, the magnitudes of the electron recombination and fine-structure cooling rates are proportional to metallicity, so regions that are heated by adiabatic and shock heating take longer to cool.

At high densities $n_H \gtrsim 10^5$ cm^{-3} where the gas is thermally coupled to the dust in the solar metallicity case there is not much

change in the supersolar metallicity case. The temperatures are slightly cooler (about 1–2 K) because the coupling is even stronger and the dust has slightly cooler temperatures due to the increased extinction. A larger effect is seen with reduced metallicities because the thermal coupling to the dust is substantially weaker. At $1/10$ solar metallicity, the gas has a maximum in the temperature distribution of about 15 K at $n_H \approx 3 \times 10^5$ cm^{-3} before the dust cooling takes over and reduces the temperatures at higher densities. At $1/100$ solar metallicity, the gas temperature rises with increasing density until $n_H \approx 2 \times 10^7$ cm^{-3} when it reaches a maximum of ≈ 20 K before it begins to drop again at higher densities.

We now consider the effects of hydrogen chemistry on the gas temperature due to heating of the gas when molecular hydrogen is formed on dust grains (equation 50). This has little effect in the calculations that began with fully molecular hydrogen (right-hand column of Fig. 22). There are two small differences. First, in the solar and supersolar calculations the upper envelope of gas temperatures is higher at densities $n_H \approx 10^2$ – 10^4 cm^{-3} . This is because some molecular hydrogen is destroyed by photodissociation and when it reforms on dust grains this adds a source of heating. Second, in the low-metallicity calculations some regions of mostly atomic gas become molecular at densities $n_H \approx 10^5$ – 10^6 cm^{-3} and the extra heating makes this gas hotter than the molecular gas at the same densities. Thus, a bifurcation of the gas temperature is apparent at these densities.

Beginning with fully atomic gas has a much greater effect on the gas temperature (centre column of Fig. 22). In these cases, heating due to H_2 formation on dust becomes significant at densities $n_H \gtrsim 10^3$ cm^{-3} , and the gas temperature is generally much greater than in the calculations without hydrogen chemistry or with fully molecular hydrogen initially. At solar and supersolar metallicities, the main effect is to raise the gas temperatures in the density range $n_H \approx 10^3$ – 10^6 cm^{-3} . Above these densities the gas is mostly molecular and the gas is thermally well-coupled to the dust. At low metallicities, the gas is significantly hotter from densities of $n_H \approx 10^3$ cm^{-3} even up to $n_H \approx 10^8$ cm^{-3} . This is primarily because of the reduced dust abundance which has two main effects: the atomic hydrogen persists to higher densities, and the gas does not become thermally coupled to the gas until much higher densities.

As mentioned above, the general temperature trends seen here are in agreement with those found by Glover & Clark (2012c). However, there are also some differences. At low densities, our temperatures tend to be lower because of the different equilibrium models that we have already mentioned (Fig. 1). But there are also differences at higher densities. In the solar metallicity cases, Glover & Clark (2012c) obtain slightly lower minimum temperatures at $n_H \sim 10^3$ cm^{-3} . This may be because their molecular cooling is somewhat stronger (cf. the difference that increasing the molecular cooling makes in Figs 17 and 19). In the calculations at $1/10 Z_{\odot}$, the mean temperatures at each density are similar to those obtained by Glover & Clark (2012c) for both atomic and molecular initial conditions, but the scatter in the temperatures obtained by Glover & Clark (2012c) is greater at $n_H \gtrsim 10^5$ cm^{-3} . This may be largely due to the different density structure of the clouds (caused by the different initial velocity fields). In the lowest metallicity calculations ($1/100 Z_{\odot}$), the temperatures obtained by Glover & Clark (2012c) are generally higher than ours at $n_H \gtrsim 10^4$ cm^{-3} for the molecular initial conditions, and above $n_H \gtrsim 10^6$ cm^{-3} for the atomic initial conditions. This may be related to the higher molecular hydrogen abundances that were commented on when we discussed Fig. 21. In our initially atomic calculation, the gas is mostly molecular for densities $n_H \gtrsim 10^6$ cm^{-3} meaning that there will be little heating

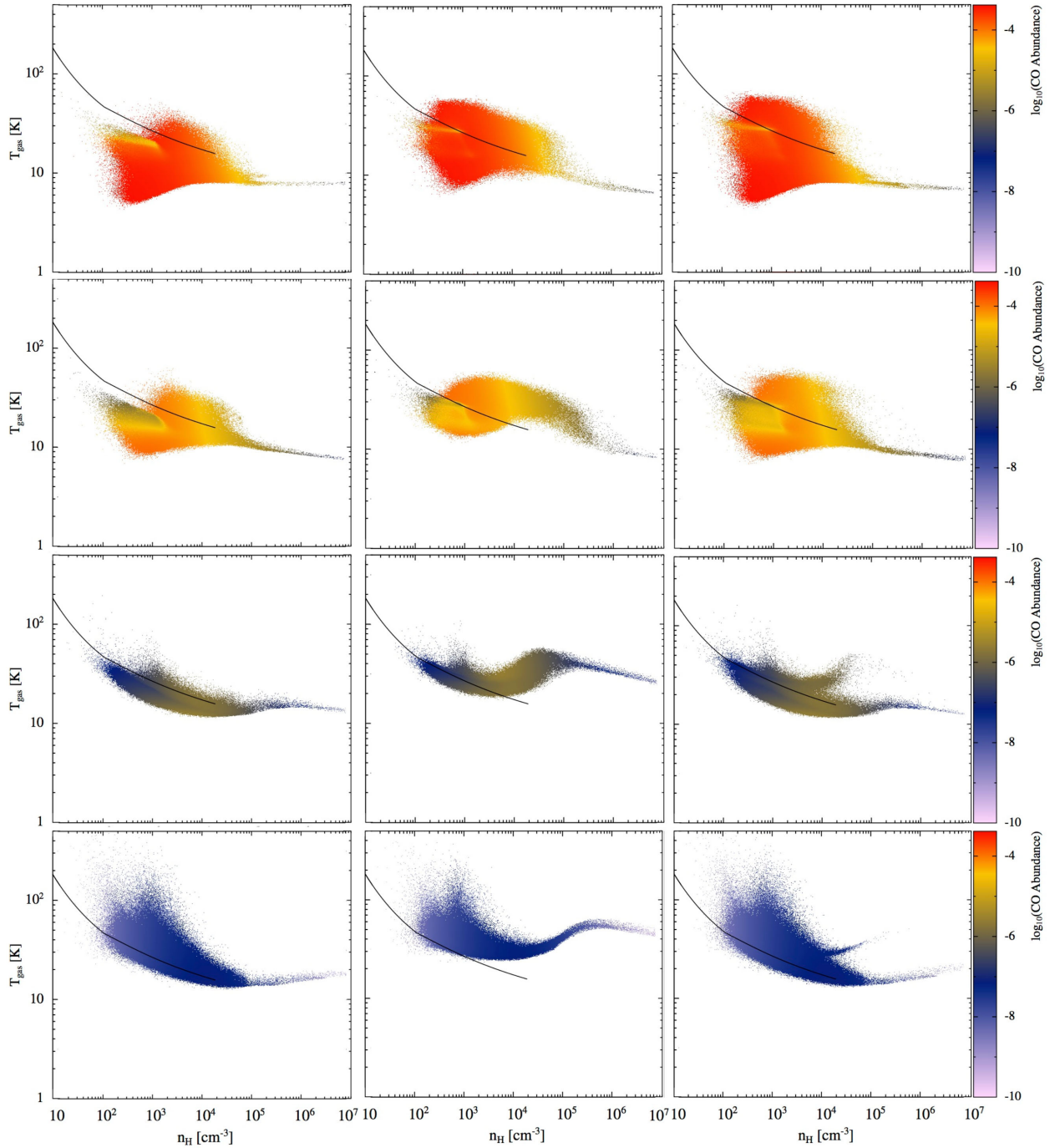


Figure 22. Phase diagrams of the gas temperature versus the gas density in turbulent clouds with metallicities of 3, 1, 1/10, and 1/100 times solar (top to bottom, respectively). The calculations in the left-hand column were performed without any H₂ chemistry (assuming purely molecular hydrogen) and without heating from H₂ formation. The other two columns included H₂ chemistry and heating from H₂ formation, but the calculations in the centre column began with fully atomic hydrogen, and the calculations in the right column began with fully molecular hydrogen. The colour bars indicate the average CO abundance of each point in temperature–density space (note that the scales differ from those in Figs 16, 17, 19, and 20). The black solid lines give the equilibrium curve from Fig. 1 for solar metallicity. Beginning with atomic gas results in significantly higher gas temperatures for densities $n_{\text{H}} \sim 10^4$ – 10^6 cm⁻³ (or even higher densities in the low-metallicity cases) due to heating from H₂ formation on dust grains.

from H₂ formation above these densities. If Glover & Clark (2012c) have more atomic gas remaining at high densities, this will provide additional heating. In our initially molecular calculation, because the stars begin to form at 2.0 Myr instead of 3.6 Myr, more of the initial molecular hydrogen remains. The total abundance is only 20 per cent in the calculation of Glover & Clark (2012c) when the

temperature diagrams were plotted, whereas the total abundance in our calculation is 60 per cent and all of the high-density gas ($n_{\text{H}} \gtrsim 10^5$ cm⁻³) is essentially fully molecular (i.e. there is little heating from H₂ formation). On the other hand, the temperature–density behaviour we obtain for the low-metallicity fully atomic initial conditions is in very good agreement with the results given

in fig. 1 of Omukai et al. (2005). For 1/10 Z_{\odot} calculations, the temperature at high densities has a peak at $n_{\text{H}} \sim 10^5 \text{ cm}^{-3}$ at similar temperatures in both our calculations and those of Omukai et al. At 1/100 Z_{\odot} , both our results and those of Omukai et al. display high-density temperature maxima of $T_{\text{g}} \approx 60 \text{ K}$ at $n_{\text{H}} \approx 10^6 \text{ cm}^{-3}$.

5 CONCLUSIONS

We have presented a new method for modelling the thermal evolution of star-forming molecular clouds. The method combines a model for the thermodynamics of the diffuse ISM with radiative transfer in the flux-limited diffusion approximation. The former is required to correctly model the thermal behaviour of molecular clouds at low densities and metallicities, while the latter allows us to model protostar formation. Unlike most previously published star formation calculations, our new model evolves the temperatures of the gas, dust, and radiation separately. The code can also follow the evolution of atomic and molecular hydrogen. We have compared our method with existing literature on the thermal behaviour of the ISM and molecular cloud cores and generally obtain good agreement.

We have also explored the sensitivity of the thermal structure of molecular cloud cores and turbulent clouds to many of the parameters that enter our diffuse ISM model. For the gas at solar metallicities, the most important thermal processes at low densities ($n_{\text{H}} \lesssim 1\text{--}1000 \text{ cm}^{-3}$) are photoelectric heating of electrons from dust grains and cooling due to electron recombination with small grains and PAHs and fine-structure emission from C^+ and atomic oxygen. At high densities ($n_{\text{H}} \gtrsim 10^5 \text{ cm}^{-3}$), cosmic ray heating and the work done by hydrodynamical flows dominate the heating, while the cooling is dominated by continuum dust emission so that the gas and dust adopt similar temperatures. At intermediate densities ($n_{\text{H}} \lesssim 10^3\text{--}10^5 \text{ cm}^{-3}$), most processes have a significant effect and there tends to be a large dispersion of temperatures in turbulent clouds. The abundance of C^+ changes rapidly at these densities and because C^+ is such an effective coolant it is important to have a model for the C^+ abundance. However, the exact values of the molecular cooling rates, molecular depletion, and the strength of the thermal coupling between the dust and the gas are less important. When beginning with low-density molecular clouds (which may not be purely molecular), the thermal evolution also depends significantly on relative abundances of atomic and molecular hydrogen due to heating from the formation of molecular hydrogen on dust grains. This becomes more important at lower metallicities.

Our new method should allow more realistic radiation hydrodynamical calculations of star formation to be performed, particularly in molecular clouds that have low mean densities ($n_{\text{H}} \lesssim 10^4 \text{ cm}^{-3}$) and/or subsolar metallicities. However, we also emphasize that this model is far from complete. In particular, it relies on various parametrizations of the thermal effects of many physical processes, and it does not calculate these processes explicitly. Furthermore, it contains only extremely simple models of hydrogen and carbon chemistries and does not explicitly model the chemistry of other elements at all. However, the basic model developed in this paper could easily be extended to increase the complexity of the chemical modelling (at the cost of increased computational expense).

ACKNOWLEDGEMENTS

We thank Paul Clark for constructive criticism that helped improve the method, and the anonymous referee whose comments

helped us improve the manuscript. This work was supported by the European Research Council under the European Community's Seventh Framework Programme (FP7/2007-2013 grant agreement no. 339248). The calculations for this paper were performed on the University of Exeter Supercomputer, a DiRAC Facility jointly funded by STFC, the Large Facilities Capital Fund of BIS, and the University of Exeter, and on the Complexity DiRAC Facility jointly funded by STFC and the Large Facilities Capital Fund of BIS.

REFERENCES

- Alexander D. R., 1975, *ApJS*, 29, 363
 Bakes E. L. O., Tielens A. G. G. M., 1994, *ApJ*, 427, 822
 Bate M. R., 2009, *MNRAS*, 392, 1363
 Bate M. R., 2010, *MNRAS*, 404, L79
 Bate M. R., 2011, *MNRAS*, 417, 2036
 Bate M. R., 2012, *MNRAS*, 419, 3115
 Bate M. R., 2014, *MNRAS*, 442, 285
 Bate M. R., Bonnell I. A., 2005, *MNRAS*, 356, 1201
 Bate M. R., Bonnell I. A., Price N. M., 1995, *MNRAS*, 277, 362
 Bate M. R., Bonnell I. A., Bromm V., 2003, *MNRAS*, 339, 577
 Bate M. R., Tricco T. S., Price D. J., 2014, *MNRAS*, 437, 77
 Benz W., 1990, in Buchler J. R., ed., *Numerical Modelling of Nonlinear Stellar Pulsations Problems and Prospects*. Kluwer, Dordrecht, p. 269
 Benz W., Cameron A. G. W., Press W. H., Bowers R. L., 1990, *ApJ*, 348, 647
 Bergin E. A., Hartmann L. W., Raymond J. C., Ballesteros-Paredes J., 2004, *ApJ*, 612, 921
 Black J. H., 1994, in Cutri R. M., Latter W. B., eds, *ASP Conf. Ser. Vol. 58, The First Symposium on the Infrared Cirrus and Diffuse Interstellar Clouds*. Astron. Soc. Pac., San Francisco, p. 355
 Black J. H., Dalgarno A., 1977, *ApJS*, 34, 405
 Boley A. C., Hartquist T. W., Durisen R. H., Michael S., 2007, *ApJ*, 656, L89
 Bonnell I. A., Bate M. R., Vine S. G., 2003, *MNRAS*, 343, 413
 Bonnell I. A., Clarke C. J., Bate M. R., 2006, *MNRAS*, 368, 1296
 Bonnell I. A., Smith R. J., Clark P. C., Bate M. R., 2011, *MNRAS*, 410, 2339
 Boss A. P., Fisher R. T., Klein R. I., McKee C. F., 2000, *ApJ*, 528, 325
 Burke J. R., Hollenbach D. J., 1983, *ApJ*, 265, 223
 Clark P. C., Glover S. C. O., Klessen R. S., 2012a, *MNRAS*, 420, 745
 Clark P. C., Glover S. C. O., Klessen R. S., Bonnell I. A., 2012b, *MNRAS*, 424, 2599
 Dobbs C. L., Bonnell I. A., 2007, *MNRAS*, 376, 1747
 Dobbs C. L., Bonnell I. A., Pringle J. E., 2006, *MNRAS*, 371, 1663
 Dopcke G., Glover S. C. O., Clark P. C., Klessen R. S., 2011, *ApJ*, 729, L3
 Dopcke G., Glover S. C. O., Clark P. C., Klessen R. S., 2013, *ApJ*, 766, 103
 Draine B. T., 1978, *ApJS*, 36, 595
 Draine B. T., Bertoldi F., 1996, *ApJ*, 468, 269
 Edgar R., Clarke C., 2003, *MNRAS*, 338, 962
 Elmegreen B. G., Klessen R. S., Wilson C. D., 2008, *ApJ*, 681, 365
 Fehlberg E., 1969, NASA Technical Report, Low-order classical Runge-Kutta formula with stepsize control and their application to some heat transfer problems. NASA, Washington, DC, R-315
 Ferguson J. W., Alexander D. R., Allard F., Barman T., Bodnarik J. G., Hauschildt P. H., Heffner-Wong A., Tamanai A., 2005, *ApJ*, 623, 585
 Glover S. C. O., 2003, *ApJ*, 584, 331
 Glover S. C. O., Clark P. C., 2012a, *MNRAS*, 421, 9
 Glover S. C. O., Clark P. C., 2012b, *MNRAS*, 421, 116
 Glover S. C. O., Clark P. C., 2012c, *MNRAS*, 426, 377
 Glover S. C. O., Mac Low M.-M., 2007a, *ApJS*, 169, 239
 Glover S. C. O., Mac Low M.-M., 2007b, *ApJ*, 659, 1317
 Glover S. C. O., Mac Low M.-M., 2011, *MNRAS*, 412, 337
 Glover S. C. O., Federrath C., Mac Low M.-M., Klessen R. S., 2010, *MNRAS*, 404, 2
 Goldsmith P. F., 2001, *ApJ*, 557, 736

- Goldsmith P. F., Langer W. D., 1978, *ApJ*, 222, 881
- Goldsmith D. W., Habing H. J., Field G. B., 1969, *ApJ*, 158, 173
- Górski K. M., Hivon E., Banday A. J., Wandelt B. D., Hansen F. K., Reinecke M., Bartelmann M., 2005, *ApJ*, 622, 759
- Habing H. J., 1968, *Bull. Astron. Inst. Neth.*, 19, 421
- Hollenbach D., McKee C. F., 1989, *ApJ*, 342, 306
- Hoyle F., 1953, *ApJ*, 118, 513
- Hunter C., 1962, *ApJ*, 136, 594
- Jappsen A.-K., Klessen R. S., Larson R. B., Li Y., Mac Low M.-M., 2005, *A&A*, 435, 611
- Jeans J. H., 1929, *The Universe Around Us*. Cambridge Univ. Press, Cambridge
- Keto E., Caselli P., 2008, *ApJ*, 683, 238
- Keto E., Field G., 2005, *ApJ*, 635, 1151
- Keto E., Rawlings J., Caselli P., 2014, *MNRAS*, 440, 2616
- Krumholz M. R., 2006, *ApJ*, 641, L45
- Krumholz M. R., 2011, *ApJ*, 743, 110
- Krumholz M. R., Klein R. I., McKee C. F., 2012, *ApJ*, 754, 71
- Larson R. B., 1969, *MNRAS*, 145, 271
- Larson R. B., 1985, *MNRAS*, 214, 379
- Larson R. B., 2005, *MNRAS*, 359, 211
- Layzer D., 1963, *ApJ*, 137, 351
- Lepp S., Shull J. M., 1983, *ApJ*, 270, 578
- Levermore C. D., Pomraning G. C., 1981, *ApJ*, 248, 321
- Low C., Lynden-Bell D., 1976, *MNRAS*, 176, 367
- Martin P. G., Schwarz D. H., Mandy M. E., 1996, *ApJ*, 461, 265
- Micic M., Glover S. C. O., Federrath C., Klessen R. S., 2012, *MNRAS*, 421, 2531
- Mihalas D., Mihalas B. W., 1984, *Foundations of Radiation Hydrodynamics*. Oxford Univ. Press, New York
- Morris J. P., Monaghan J. J., 1997, *J. Comput. Phys.*, 136, 41
- O'Donnell E. J., Watson W. D., 1974, *ApJ*, 191, 89
- Offner S. S. R., Klein R. I., McKee C. F., Krumholz M. R., 2009, *ApJ*, 703, 131
- Omukai K., 2000, *ApJ*, 534, 809
- Omukai K., Tsuribe T., Schneider R., Ferrara A., 2005, *ApJ*, 626, 627
- Ossenkopf V., Henning T., 1994, *A&A*, 291, 943
- Pavlyuchenkov Y. N., Zhilkin A. G., 2013, *Astron. Rep.*, 57, 641
- Pavlyuchenkov Y. N., Zhilkin A. G., Vorobyov E. I., Fateeva A. M., 2015, *Astron. Rep.*, 59, 133
- Pollack J. B., McKay C. P., Christofferson B. M., 1985, *Icarus*, 64, 471
- Preibisch T., Sonnhalter C., Yorke H. W., 1995, *A&A*, 299, 144
- Price D. J., Bate M. R., 2007, *MNRAS*, 377, 77
- Price D. J., Monaghan J. J., 2005, *MNRAS*, 364, 384
- Price D. J., Monaghan J. J., 2007, *MNRAS*, 374, 1347
- Rees M. J., 1976, *MNRAS*, 176, 483
- Rozycka M., 1983, *A&A*, 125, 45
- Shapiro P. R., Kang H., 1987, *ApJ*, 318, 32
- Tielens A. G. G. M., 2005, *The Physics and Chemistry of the Interstellar Medium*. Cambridge Univ. Press, Cambridge
- Tohline J. E., 1980, *ApJ*, 239, 417
- Turner N. J., Stone J. M., 2001, *ApJS*, 135, 95
- Whitehouse S. C., Bate M. R., 2006, *MNRAS*, 367, 32
- Whitehouse S. C., Bate M. R., Monaghan J. J., 2005, *MNRAS*, 364, 1367
- Whitworth A. P., Boffin H. M. J., Francis N., 1998, *MNRAS*, 299, 554
- Witt A. N., Johnson M. W., 1973, *ApJ*, 181, 363
- Wolfire M. G., Cassinelli J. P., 1987, *ApJ*, 319, 850
- Wolfire M. G., McKee C. F., Hollenbach D., Tielens A. G. G. M., 2003, *ApJ*, 587, 278
- Yorke H. W., Sonnhalter C., 2002, *ApJ*, 569, 846
- Young C. H. et al., 2004, *ApJS*, 154, 396
- Zucconi A., Walmsley C. M., Galli D., 2001, *A&A*, 376, 650

This paper has been typeset from a $\text{\TeX}/\text{\LaTeX}$ file prepared by the author.